4. Neutron Scattering

The neutron scattering program of the Solid State Division continues to exploit the neutron beams of the High Flux Isotope Reactor (HFIR) and the Oak Ridge Research Reactor (ORR) to obtain fundamental microscopic information on condensed matter. Such information is very important for increasing our knowledge of solid state science and for providing assistance in solving the long-range energy-related problems of our country. The beams at the HFIR are the most intense thermal-neutron beams for research in the world, and the experimental facilities associated with them provide powerful, and in some cases, unique tools for materials science research. All four horizontal beam tubes are now equipped with a main and a satellite instrument. The two additions during the past year are (1) the low-energy triple-axis spectrometer at HB-1 and (2) the perfect double crystal small-angle scattering apparatus at HB-3. Plans are being formulated to place two additional instruments on the engineering facility level with neutron beams scattered vertically from HB-1 (high resolution powder diffractometer) and from HB-4 (high intensity–long flight path, small-angle neutron scattering instrument).

For much of the past year the ORR has run on a drastically reduced schedule. Nevertheless, significant progress in the construction, installation, and operation has been achieved of a small-angle neutron scattering instrument that utilizes a two-dimensional position-sensitive detector. If, as seems probable, the ORR resumes full-time operation in FY 1978, beam ports HB-1 and HB-2 will be instrumented with a triple-axis crystal spectrometer and a polarized beam diffractometer, respectively, and the applications of the wide angle–long wavelength instrument at HB-3 to magnetic diffuse scattering studies will be reactivated.

As in past years, because of the properties (energy, momentum, magnetic moment) of neutrons that are exploited in scattering experiments, the neutron scattering research of the Division falls generally into the areas of lattice dynamics and magnetic properties. For convenience the research results that appear in this section have been divided into these two areas and a third containing results from small-angle neutron scattering experiments; the latter division reflects the growing emphasis of the program in exploiting the small-angle scattering technique to obtain information about long-range scattering density fluctuations. Other equally good divisions could be made that would reflect the concentration of the research into specific problem areas. It will be noted that many of the problems investigated have as a primary aim the acquisition of fundamental information related to energy production, storage, and transmission, a trend that was already marked last year and which no doubt will continue in future years. Examples of some recent investigations are summarized in the following paragraphs.

A very important area of solid state physics to which neutron scattering methods can be applied is the study of defects. The term is used here in the broadest sense to include any departure from pure and perfect materials. Perturbations of the phonon spectra of pure metals by very light or very heavy impurities, the dynamics and diffusion of hydrogen in metals, and the size, shape, and distribution of radiation-

induced voids in reactor materials are all under study. During the past year a comprehensive study of the temperature dependence of phonon-defect mode hybridization in KCl:CN has been carried out. These studies have significance not only in themselves as prototype molecular defect studies but also in application (1) to interpretations of experiments on radiation-induced split interstitials in copper and aluminum and (2) to the mechanism of conductivity in superionic conductors, the silver halides in particular. The CN^- radical, when placed in potassium chloride as a substitutional impurity, is a complex defect which exhibits a wide variety of motions—tunneling, libration, free rotation. Phonons can interact with the molecular motions, and a study of the temperature dependence of the interactions for phonons of various symmetries can provide information about the molecular energy states and wave functions.

In the past few years the study of the properties of mixed valence systems has been an extremely active area. Compounds of samarium, in particular, have been actively investigated, as have metallic cerium and its intermetallic compounds. Under pressure, or when appropriately alloyed, SmS changes from an insulating black phase to a metallic gold phase. This is accompanied by a change in volume, which is thought to be due to a change in the configuration of the samarium ion. Depending upon the nature of the probes used and the corresponding time scale of the measurements, one can conclude that the metallic state consists of (1) a mixture of Sm^{2+} and Sm^{3+} ions or (2) a homogeneous state with properties intermediate between those of the two free ions. Currently it is thought that the true picture is one involving rapid fluctuations between these two states with a characteristic time that turns out to be ideal for neutron scattering experiments. Three types of experiments on SmS and $Sm_xY_{1-x}S$ are in progress in an attempt to understand these substances and mixed valence systems generally. Measurements of the phonon spectra, of the crystal field energy spectrum, and of the magnetic form factor have been carried out. For the first time a direct observation of the valence fluctuation rate has been made.

A rather old area of investigation, magnetic moment distribution in ferromagnetic alloys, has received new emphasis in the last few years through the application of both polarized and nonpolarized beam methods to the same specimens. Recent measurements on nickel-copper alloys have been interpreted in terms of a magnetic environment model in which the nickel moments are functions of the moments of neighboring atoms. The model has been extended to systems in which both types of atoms carry moments (nickel-rhodium) for which both chemical and magnetic environment effects are important. This model appears general enough and flexible enough to account for the properties of alloys in the iron-aluminum system, the palladium-manganese system, and for alloys of iron with other 3*d* transition metals. Measurements of this type are carried out in this country only at Oak Ridge National Laboratory.

It should be emphasized that the solution to a given problem is sought by all possible means and with all experimental tools available to Division members. A very close and important interaction exists between members of the Neutron Scattering Program, the Solid State Theory Program, and the Superconductivity Program. An equally close relationship exists with members of the Research Materials Program, who have provided well-characterized single-crystal specimens for many of the neutron scattering investigations reported here.

SMALL-ANGLE NEUTRON SCATTERING

SMALL-ANGLE NEUTRON SCATTERING INSTRUMENT WITH A TWO-DIMENSIONAL POSITION-SENSITIVE DETECTOR

H. R. Child S. Spooner[1]

During the past year, a new small-angle neutron scattering instrument has been installed and tested at HB-6, Oak Ridge Research Reactor (ORR). This machine has several novel features and will allow small-angle scattering experiments to be performed at once. In addition, it is intended to serve as a feasibility study for a larger, more complete unit that we hope can be installed at the higher flux HFIR.

Figure 4.1 is a schematic diagram of the apparatus. The heart of the new system is a two-dimensional position-sensitive proportional counter of the Kopp-Borkowski[2] type which allows the entire scattered intensity around $2\theta = 0$ to be detected simultaneously, thus increasing the effective intensity. The detector is placed in the direct beam with a cadmium beam stop positioned to intercept the transmitted neutrons. Such a position has not only the advantage of showing the symmetry of the scattered radiation around a zero scattering angle but also that of increasing the effective scattered intensity for isotropic scattering by a factor of 4 from the four quadrants measured at once. Filled to about 2 atm with ^{3}He, Xe, and Ar, the detector is about 60% efficient. The active area of 20 cm × 20 cm is resolved into 32 × 32 or 64 × 64 channels in the x and y directions giving spatial resolution of 0.63 cm or 0.31 cm respectively.

The neutrons from the reactor core are filtered through 12 cm of beryllium metal cooled to 77 K and monochromatized by reflection from three pyrolytic graphite crystals scattering by Bragg reflection at about 88, 90, and 92° to select a central wavelength of 4.74 Å with about 5% resolution. These neutrons are then diffracted again by three more matched crystals to bring the beam back parallel to, but displaced from, the first beam and out of the reactor shield. A 7-m evacuated flight tube carries the incident neutron beam to a sample through a circular, 1-cm-diam B_4C slit. The detector can be positioned at either 1 or 5 m from the sample because evacuated scattering tubes are presently available in these lengths; other distances can be obtained in the future.

These dimensions provide a visible region of $\kappa = (4\pi \sin \theta)/\lambda$ of about 6 to 40 × 10^{-3} Å^{-1} at 5 m and about 14 to 145 × 10^{-3} Å^{-1} at 1 m with a resolution limited by the beam size of 1 cm diam at present so that

$$\Delta\kappa = \frac{4\pi \sin \theta}{\lambda} \frac{1}{2} \frac{1}{100} \cong 3 \times 10^{-3} \text{ Å}^{-1}$$

at 5 m and 13 × 10^{-3} Å^{-1} at 1 m, both of which are larger than the incident resolution.

The x, y position information of a pulse is converted to a channel address by an interface circuit designed by E. Madden of the Instrumentation and Controls Division, and the proper memory location

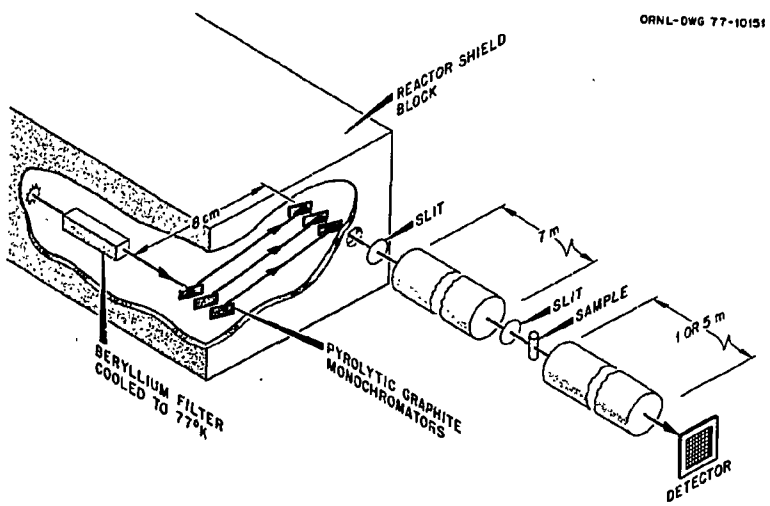

Fig. 4.1. Schematic diagram of small-angle neutron scattering instrument installed at HB-6, ORR.

in a 16-bit HP-21MX on-line computer is incremented to record the event. The computer also provides an essentially live display of the counts on a 5-in. oscilloscope that can display either a contour-shaped image of the accumulated counts in the detector or any x or y slice across the detector. The data can be accumulated either vs time or vs incident beam flux by means of a low-efficiency fission counter located just off center of the beam path in front of the incident slit. A magnetic tape unit allows data to be stored temporarily, but the limited memory of the computer (16 K) restricts on-line data analysis severely. The data are usually punched on a high-speed paper tape for further analysis and processing on the PDP-10 or on the IBM-360 computers. Fortran programs for most of the analyses desired are available, and more are being accumulated. Because each run produces many numbers, some form of computer analysis is required immediately.

Although the ORR has been operated on a much-reduced schedule during most of the period covered by this report, some results from this new scattering facility have been obtained. Some of the more extensive of these results are discussed in other papers in this report, but we have also conducted preliminary studies of catalyst support materials, polymers, and metallurgical problems in copper-titanium, lead, and nickel-aluminum alloys. As an example, Fig. 4.2 shows relative intensity data for deuterated polyethylene in both powder and solid forms averaged over the direction of κ. Although the scale of intensities cannot be directly compared, the falloff with κ does give some information for the two samples. If an analysis in terms of a radius of gyration of the scattering entities is done from these data, values of $R_g = 39$ Å and 150 Å are obtained for the solid and powder specimens respectively. These values are obtained from the slope of $\ln I(\kappa)$ vs κ^2 at the smallest κ where the radius of gyration concept is most suitable, but if similar slopes at larger κ are compared, the radius of gyration is 55 ± 1 Å for both samples. This latter value may reflect the true size of the polymer chains in this material, although the interpretation of the radius of gyration is somewhat unclear in polymer studies.

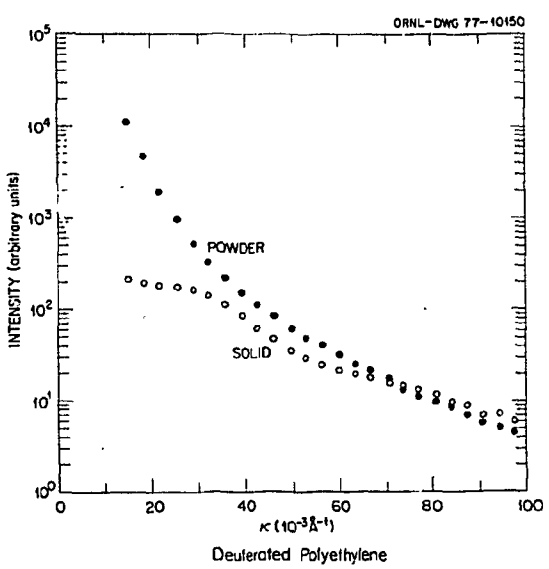

Fig. 4.2. Intensity vs $\kappa = (4\pi \sin\theta)/\lambda$ for solid and powdered deuterated polyethylene.

1. Consultant from Georgia Institute of Technology, Atlanta.
2. M. K. Kopp and C. J. Borkowski, *Position-Sensitive Proportional Counters Using Resistance-Capacitance Position Encoding*, ORNL/TM-5083 (December 1975); C. J. Borkowski and M. K. Kopp, *IEEE Trans. Nucl. Sci.* NS-17, 340 (1970); C. J. Borkowski and M. K. Kopp, *IEEE Trans. Nucl. Sci.* NS-19, 161 (1972).

SMALL-ANGLE NEUTRON SCATTERING STUDY OF FACETTED VOIDS WITH THE BORKOWSKI-KOPP AREA-SENSITIVE PROPORTIONAL COUNTER

S. Spooner[1] H. R. Child

The Borkowski-Kopp area proportional detector has been successfully applied to the measurements of neutron scattering from facetted octahedra voids in a reactor-irradiated single crystal of aluminum. The sample is one of the series of aluminum samples studied by Mook[2] and by Hendricks and Schelten[3] in which swelling of approximately 0.6% was produced. Scattering asymmetries were noted in both x-ray work[4] and neutron work[3] and have been quantitatively measured with a linear detector technique.[5] In the present work, the detector (20 cm × 20 cm) was brought in close to the specimen to pick up an angular range of scattering that would show the asymmetry. A qualitative comparison between the theoretical predictions and the experiment is shown (Fig. 4.3). Differences are indicated which suggest that the degree of truncation may be different from that observed by Hendricks and Schelten.[3] Figure 4.4 illustrates the scattering asymmetry observed for two crystal orientations.

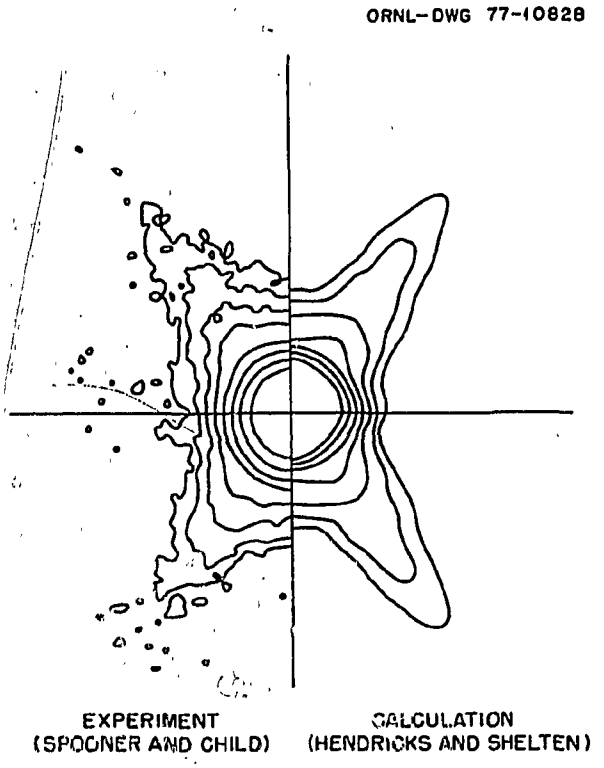

Fig. 4.3. A comparison between calculated (ref. 2) and measured area detector pattern.

Analysis of the data is proceeding on the question of void size distribution. Spherically averaged data are being obtained on the same specimen. The crystal is rotated in the beam on its cylindrical axis, and the accumulated area detector data are then radially averaged. By this approach it is anticipated that data having more precision can be used in the determination of void size distribution. An analysis of the truncation effects is being undertaken by "curve-fitting" between calculated and measured area detector data. The spherically averaged data are expected to yield the size distribution coefficients that are used to calculate the observed scattering from a polydispersed collection of truncated octahedra voids. This void structure analysis problem will be an informative exercise in assessing the practical aspects of area detector data analysis.

1. Consultant from Georgia Institute of Technology, Atlanta.
2. H. A. Mook, *J. Appl. Phys.* **45**, 43 (1974).
3. R. W. Hendricks, J. Schelten, and W. Schmatz, *Philos. Mag.* **30**, 819 (1974).
4. J. E. Epperson, R. W. Hendricks, and K. Farrell, *Philos. Mag.* **30**, 803 (1974).
5. R. W. Hendricks, J. Schelten, and G. Lippman, *Philosophical Magazine* (to be published).

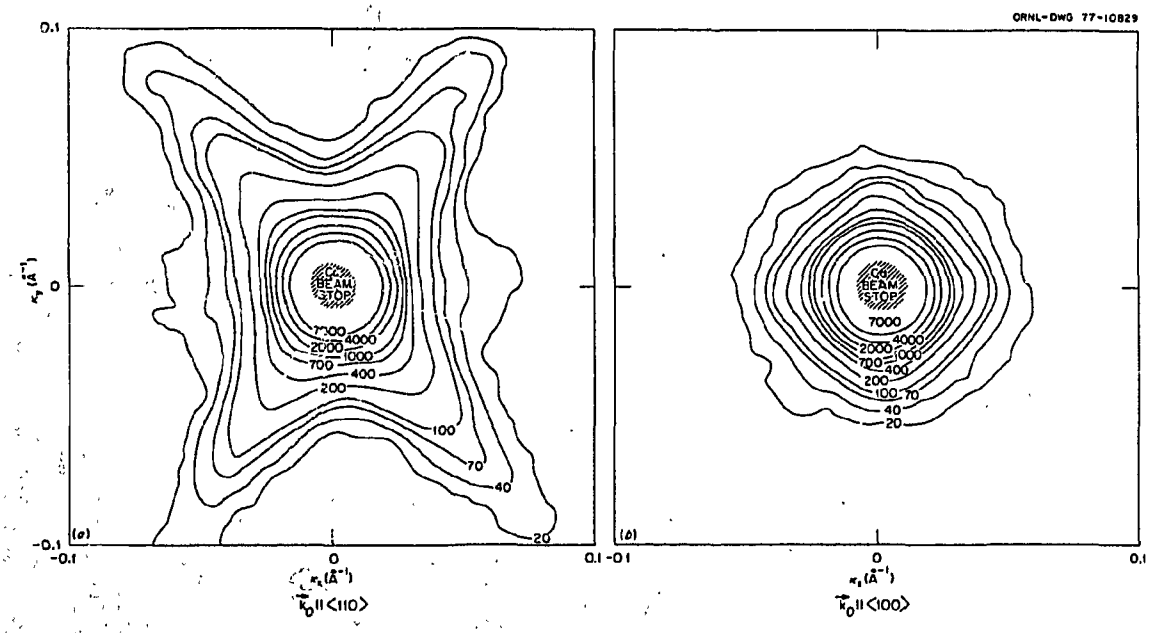

Fig. 4.4. Area detector patterns arising from facetted octahedra voids: (*a*) k_0 parallel to [110], (*b*) k_0 parallel to [100].

SMALL-ANGLE NEUTRON SCATTERING OF REACTOR-IRRADIATED NIOBIUM

S. Spooner[1] H. R. Child

Polycrystalline niobium samples that were irradiated in the EBR-II were the object of small-angle neutron scattering (SANS) study for corroboration of electron microscopy and density measurements. This problem represented a difficult challenge because of small void sizes and small specimen thickness (0.020 in.). In one specimen, electron diffraction indicated an ordered void configuration; we watched for some SANS evidence of this effect. The scattering curves were obtained by radial averaging of the area detector data. In two of the specimens a clear indication of a duplex population of void sizes was shown. A plot of the log of intensity vs K^2 revealed a clear transition from one slope to another (Fig. 4.5*a* and *b*). The analysis was done by curve fitting to a four-parameter model in which the data were represented by the sum of two Gaussian curves. The Guinier radii and relative extrapolated intensities for each specimen are summarized (Table 4.1). While it is conceded that the analysis is not very precise because of the data statistics, it is pointed out that only area detector data collection would be capable of achieving this analysis at all. The correspondence between the SANS results and electron microscopy is very satisfactory. However, no void interference effects were observed in the scattering pattern from the sample that showed a void lattice. This negative result could arise from inadequate intensity. The spherical averaging in a polycrystalline sample reduces the interference peak. Alternatively the electron microscopy result might not be representative of the average sample. Further analysis of these data is proceeding.

1. Consultant from Georgia Institute of Technology, Atlanta.

Table 4.1. Analysis of niobium voids

Alloy identification	Guinier radius	Intensity
G-15-Nb-1-Zr-10	168 ± 6 Å	1780 ± 310
	38 ± 2 Å	44 ± 3
G-15-Nb-1-2	83 ± 3 Å	210 ± 10
	34 ± 5 Å	24 ± 6
C-15-Nb-1-1	30 ± 5 Å	30 ± 2

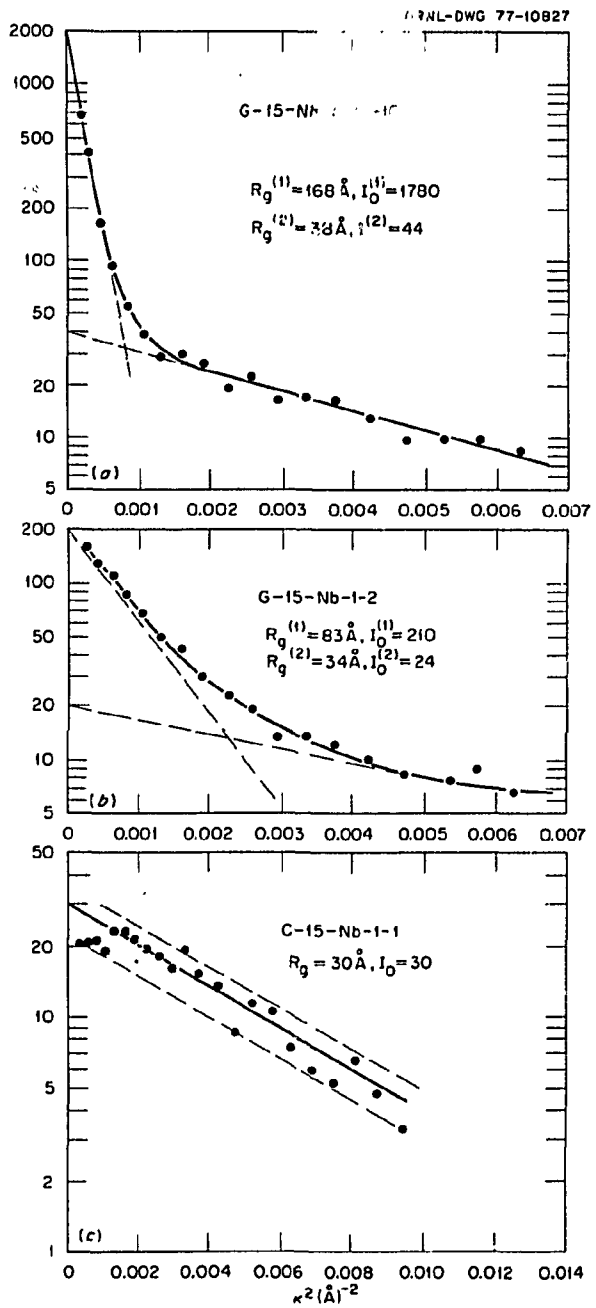

Fig. 4.5. Radially averaged area detector data, corrected for background. (*a*) Sample G-15-Nb-1-Zr-10, (*b*) Sample G-15-Nb-1-2, (*c*) Sample C-15-Nb-1-1.

SMALL-ANGLE NEUTRON SCATTERING FROM IRRADIATED TYPE 304 STAINLESS STEEL

H. R. Child S. Spooner[1]

Preliminary results designed to investigate void distributions in irradiated materials by small-angle

neutron scattering have been obtained from the new SANS instrument at HB-6, ORR. Some of these are discussed in other papers in this report; this paper will report such results from stainless steel.

Figure 4.6 shows intensity data obtained by averaging the counts from the position-sensitive detector as a function of constant radius from the main beam at $\kappa = 0$. Such an average gives an effective increase in intensity because it includes many channels in each data point and the errors of the data shown are smaller than the size of the points in the figure. An average of this type is only used, of course, if the scattering shows circular symmetry around the main beam. These data were obtained at the 5-m scattering path with the incident beam striking one of the upper corners of the detector. This arrangement increased the visible range of κ about a factor of 2 at the cost of measuring intensity in only one quadrant of the scattering pattern.

Two specimens of type 304 stainless steel cut from a thimble of a reactor control rod were obtained from the Metals and Ceramics Division; the two gave virtually identical SANS patterns. The specimens taken from the midreactor plane of a control rod were irradiated at 400°C to an integrated flux of about 1.6×10^{23} neutrons/cm^2 ($E > 0.1$ MeV). The samples were approximately 1 mm thick and were highly radioactive (about 2 R at contact of ^{60}Co gamma activity), which would have caused difficulty for small-angle x-ray study but represented only minor personnel shielding problems for the neutron work.

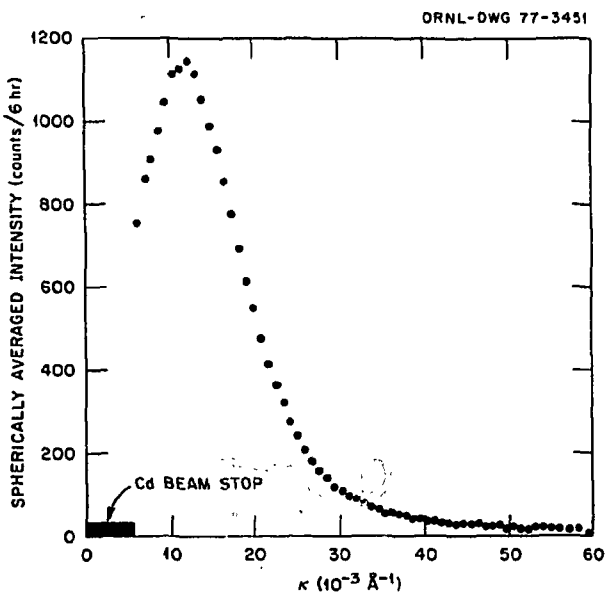

Fig. 4.6. Spherically averaged small-angle neutron scattered intensity from an irradiated stainless steel specimen.

Bloom et al. have reported electron microscope work[2] on similar samples of stainless steel which showed total void concentrations of about 10^{16} voids per cubic centimeter with a void distribution centered around a diameter of approximately 280 Å. The maximum in $I(\kappa)$ at nonzero κ shown in our data is believed to be an interference effect because the voids tend to locate at an average distance $2R_x$, where R_x represents an exclusion radius within which voids tend to avoid each other. Guinier and Fournet[3] give formulas for $I(\kappa)$ for spherical particles with interference effects between them; we have fit our data to an approximate parameterized form of these equations by least squares. The fit gives $2R_x = 240$ Å in reasonable agreement with the average diameter observed in the microscope work and with a void distribution centered about a radius of about 85 Å, which is somewhat smaller than Bloom et al. found. However, to obtain a reasonable fit, a separate void distribution centered around $R = 40$ Å is required to account for the slowly falling tail seen in the $I(\kappa)$ curve for $\kappa \gtrsim 35 \times 10^{-3}$ Å. This second void distribution was not seen in Bloom's work, but this radius may be below the limit of observation.

We hope to extend this investigation to larger values of κ to observe the κ^{-4} dependence expected in $I(\kappa)$ at sufficiently large κ and to investigate samples under other irradiation conditions.

1. Consultant from Georgia Institute of Technology, Atlanta.
2. E. E. Bloom, J. O. Stiegler, and C. J. McHargue, *Radiat. Eff.* 14, 231 (1972).
3. A. Guinier and G. Fournet, *Small-Angle Scattering of X Rays*, Wiley, New York, 1955.

A HIGH-RESOLUTION TABLE FOR DOUBLE-PERFECT CRYSTAL SMALL-ANGLE NEUTRON SCATTERING

D. K. Christen F. Tasset[1] E. W. Chandler[2]

Small-angle neutron scattering is a very useful tool for the study of fluxoid lattices in type-II superconductors. In particular, the parallel double-perfect crystal technique can provide unprecedented precision for some aspects of this application.[3]

To apply the technique successfully, one must be able to measure scattering angles by rotation of the analyzer crystal about a vertical axis. These angles must be typically determined over the range 0 to

±1000 arc sec (0 to ±4.8 millirads), with an absolute accuracy of ±0.5 arc sec and a repeatability to ±0.5 arc sec.

To meet these specifications, we have designed and constructed an automatic rotation table (Fig. 4.7, top view). It consists of a stationary arm assembly, on which a micrometer drive assembly freely floats. The drive assembly houses a digital stepping motor, linked through a 15:1 precision gear reduction box to the lead screw of a 0.0001-in. resolution micrometer. The entire floating micrometer assembly pivots, on the one end, about a fixed point on the stationary table by means of a ball bearing and seat at the rear end of the gear box output shaft. On the other end, the micrometer body is attached to a pivot point at the end of the protractor arm, exactly 20.626 in. from the vertical axis of rotation of the arm. In this way, a 0.0001-in. increment in the horizontal motion of the micrometer body yields a 1-arc-sec angle of rotation at the protractor arm axis (on this axis is the analyzer crystal poition). Because no transverse motion of the protractor axis can be tolerated, the protractor arm assembly rotates on precision-tapered roller bearings, which are loaded to eliminate any lateral free play.

An independent calibration on the relation of rotation angle to stepping motor increments has been accomplished by use of a high-precision autocollimator, which determines the angle by reflection of a light beam from a mirror placed at the analyzer crystal position. In practice, small-amplitude (approximately 1 arc sec) oscillations in the angle about its expected value are observed. These oscillations have the periodicity of the micrometer and gear box output shaft, are repeatable, and thus are corrected for in the final data reduction.

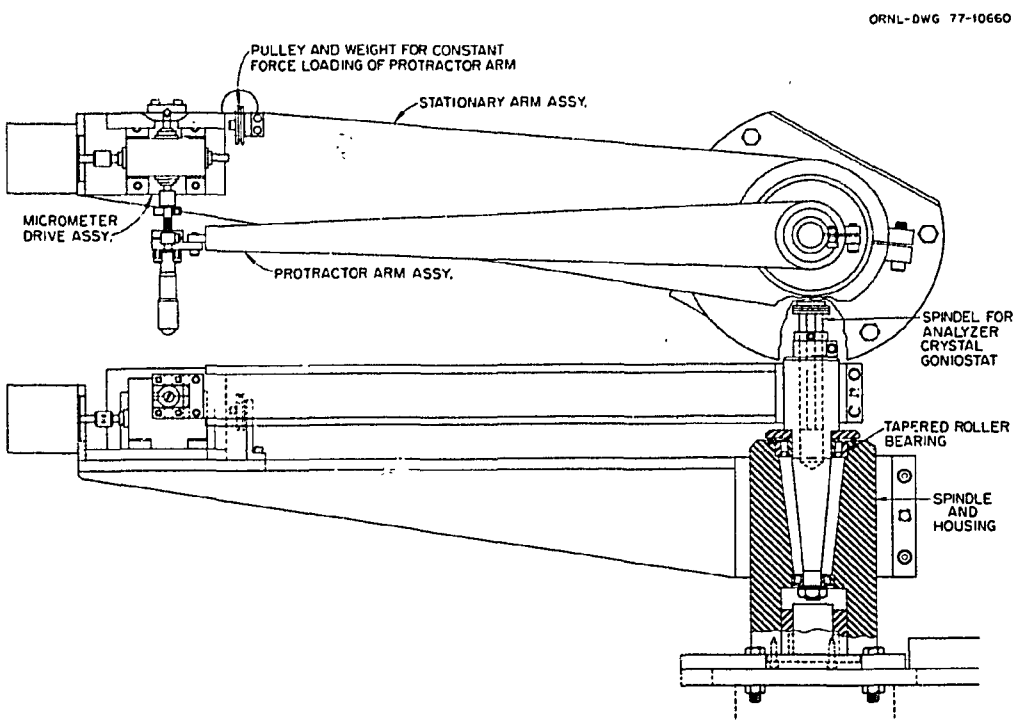

Fig. 4.7. Top view of high-resolution rotation table.

1. Guest scientist from Institut Laue-Langevin, Grenoble, France.
2. Plant and Equipment Division, ORNL.
3. D. K. Christen et al. *Phys. Rev. B* 15, 4506 (1977).

SMALL-ANGLE, DOUBLE-SILICON CRYSTAL NEUTRON DIFFRACTION STUDIES OF THE FLUX LINE LATTICE IN SUPERCONDUCTING NIOBIUM[1]

F. Tasset[2] S. Spooner[3]
D. K. Christen H. A. Mook

A novel experimental technique and a large spherical single crystal of pure niobium have enabled quantitative neutron diffraction investigations to be made of flux line lattices (FLL) in and near the intermediate mixed state. The high angular res-

olution afforded by this technique permits accurate flux density determinations. In addition, diffracted neutron-integrated intensities are found to depict bulk magnetization hysteresis, while bulk structural differences in the FLL are indicated by the angular full width at half maximum (FWHM) of the FLL rocking curves.

---

1. Abstract of paper: p. 481 in *Proceedings of the Conference on Neutron Scattering*, vol. I, ed. by R. M. Moon, ERDA CONF-760601-P1, Oak Ridge, Tenn., 1976.
2. Guest scientist from Institut Laue-Langevin, Grenoble, France.
3. Consultant from Georgia Institute of Technology, Atlanta.

LOW-FIELD ANISOTROPY OF THE FLUX LINE LATTICE IN SUPERCONDUCTING NIOBIUM

D. K. Christen S. Spooner[1] H. R. Kerchner

The structure, symmetry, and static behavior of the two-dimensional quantized FLL, which results in the mixed state of a type-II superconductor, can be studied quantitatively on the microscopic level by means of small-angle neutron scattering. A high-resolution silicon double-crystal diffractometer, previously described,[2] has been used to investigate some FLL properties in the regime of an attractive fluxoid interaction. This attractive interaction, due to nonlocal electrodynamical effects, occurs only in low-κ type-II materials (of which niobium is an example), and has been the subject of recent theoretical interest.[3,4]

For these studies, a single-crystal sphere (14 mm diam) of pure niobium was oriented to provide various high-symmetry crystalline axes parallel to an applied magnetic field H_a. Because of the spherical demagnetizing geometry, the first-order magnetic phase transition, which occurs at $H_a = H_{c1}$ for an infinite material, is broadened to result in an intermediate-mixed-state (IMS) region for $^2/_3 H_{c1} \leqslant H_a \leqslant {}^2/_3 H_{c1} + {}^1/_3 B_0$. In the IMS, the sample is filled with domains of constant-cell-size FLL, in equilibrium with flux-free Meissner regions. Here $B_0 = \phi_0/A_c$ is the equilibrium attractive flux density determined by the (constant) FLL cell area A_c and the magnetic-flux quantum ϕ_0. Thus, B_0 may be determined experimentally, at a microscopic level, by measurement of the FLL cell area A_c in an IMS-field region. This procedure is carried out by a determination of the Bragg scattering angle $2\Theta = \lambda/d$, due to diffraction of neutrons from FLL planes of spacing d, for various reflections obtained by rotating the sample about the field direction.[2] In addition, it has been pointed out that, on the microscopic level, the applied-field boundary, $H_a = {}^2/_3 H_{c1} + {}^1/_3 B_0$, between the mixed state and IMS is sharply defined. Neutron diffraction is sensitive to this transition because the FLL cell area is constant in the IMS, whereas it changes with applied field in the mixed state. A particular technique employed here is very sensitive to this transition. The diffractometer is set up to accept neutrons only at the scattering angle 2Θ, which is characteristic of the IMS. Then the neutron intensity is recorded, as H_a is incremented from the mixed state to the IMS. In this way, the neutron intensity is seen to peak sharply at the transition field, because of the changing FLL cell area in the mixed state and the changing volume fraction of constant-cell-size FLL in the IMS. The statistical error in determining the transition field $H_a = {}^2/_3 H_{c1} + {}^1/_3 B_0$ in this way is about ± 3 Oe. This field determination, in conjunction with the independent measurement of B_0, uniquely defines the lower critical field H_{c1}.

Systematic investigations of these critical parameters and of the FLL symmetry have been performed as a function of temperature and of sample orientation with respect to the applied field. In general, the anisotropic effects in B_0 and H_{c1} are observed to be small, whereas rather marked dependencies in the FLL symmetry are seen. For example, Fig. 4.8 shows how the FLL nearest-neighbor distance, a, varies with temperature and crystal orientation. In all cases, the FLL nearest-neighbor direction is parallel to niobium crystalline $\langle 110 \rangle$ axes. With the exception of the case for $H_a \parallel \langle 100 \rangle$, the FLL possessed the same symmetry properties as the real crystal. For the fourfold case, the sample was occupied by two identical distorted lattices, one oriented 90° with respect to the other. For $T \gtrsim 5$ K, these two lattices became twofold symmetric and approached the hexagonal symmetry as $T \rightarrow T_c$. With lower temperatures, the distorted lattices tended to shear in such a way as to approach a square lattice, although this state was never completely achieved down to $T = 2.0$ K.

Interestingly, the anisotropy in B_0 is very small (a maximum 0.5% effect) and of the opposite sense as that observed in the nearest-neighbor separation. That is, the FLL cell area A_c is slightly larger for the orientation that possesses the smaller FLL nearest-neighbor distance. Furthermore, the orientation dependence of H_{c1} is opposite to that of B_0 and is typically of maximum magnitude 2.5% at $T = 4$ K.

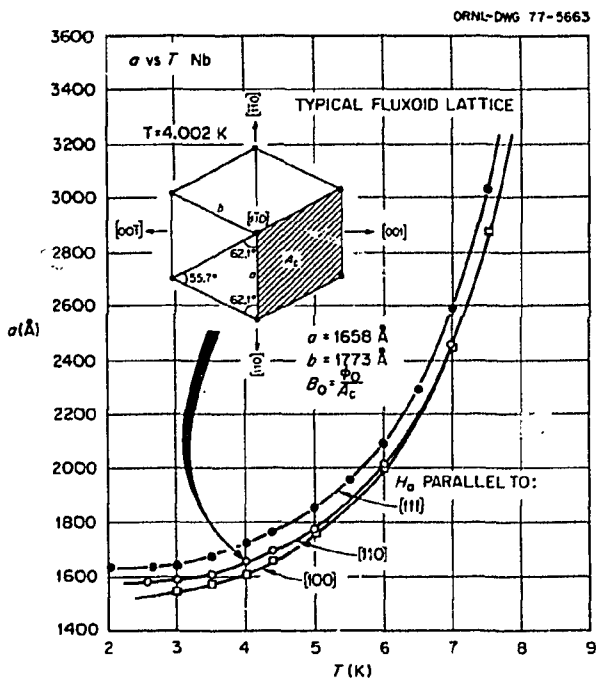

Fig. 4.8. The flux line lattice nearest-neighbor distance as a function of temperature and crystal orientation with respect to the applied field H_a.

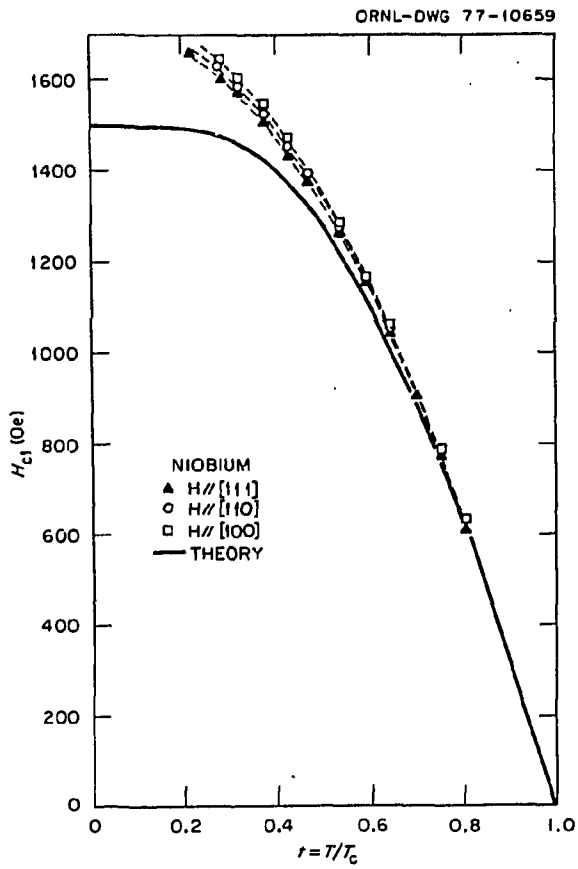

Fig. 4.9. Comparison of the theoretical isotropic H_{c1} of Shapira et al. (ref. 3) with the experimental data.

Although fundamental calculations of low-field anisotropy effects are lacking, some theoretical data for the isotropic limit are available. Figure 4.9 is a comparison of the H_{c1} data with theory.[3] Apparently the most disparity occurs at low T, while the agreement is generally good above 6 K.

These data are the first obtained with the necessary resolution to reveal the anisotropic behavior in the low-field parameters B_0 and H_{c1}. This information, coupled with the FLL symmetry properties, should provide a definitive test for the newly emerging models of anisotropic fluxoid interactions and the attractive fluxoid interaction.

---

1. Consultant from Georgia Institute of Technology, Atlanta.
2. D. K. Christen et al., *Phys. Rev. B* 15, 4506 (1977).
3. I. Shapira, M. N. Shah, and H. Umezawa, *Physica* **84B**, 213 (1976).
4. E. H. Brandt, *Phys. Status Solidi B* 77, 105 (1976).

ANISOTROPY OF THE MAGNETIZATION OF SUPERCONDUCTING NIOBIUM

H. R. Kerchner D. K. Christen S. T. Sekula

We have measured the field derivative of the magnetization (dM/dH) of a high-purity, single-crystal niobium sphere with the applied magnetic field parallel to three high-symmetry crystalline axes. The Meissner state, the intermediate mixed state, the mixed state, and the normal state show up as distinct field regions of the dM/dH vs H plots, separated by three discontinuities in dM/dH. These discontinuities occur at the fields $H_1 = \frac{2}{3}H_{c1}$, $H_2 = \frac{2}{3}H_{c1} + \frac{1}{3}B_0$, and H_{c2}, where H_{c1} and H_{c2} are the lower and upper critical fields and B_0 is the equilibrium flux density at H_{c1}. Thus the parameters H_{c1}, B_0, and H_{c2} can be determined by measuring the fields at which the discontinuities occur.

By numerically integrating the measurements twice with respect to field between H_2 and H_{c2}, we obtain the magnetization $M(H)$ and the Gibbs free energy $G(H)$. The value of $M(H_2)$, along with the measurement of H_2, provides values of H_{c1} and B_0 that are independent of the measurement of H_1. Also, the thermodynamic critical field H_c can be obtained from $G(H_2)$.

The value of dM/dH is directly related to two other parameters of interest, the generalized

Ginzburg-Landau parameter κ_2 and the compressional modulus of the flux line lattice $C_L(B)$. We analyzed the data to obtain the temperature and crystal-orientation dependences of H_{c1}, H_{c2}, B_0, κ_2, and $C_L(B_0)$, and the temperature dependence of H_c.

A field-sweep technique was used to make direct, continuous measurements of dM/dH. The sample was placed in one of two identical pickup coils that were connected in series opposition. When the magnetic field was swept at a constant rate, the induced voltage in the pickup coil was proportional to dM/dH. This low-level voltage was chopped by a metal oxide semiconductor field-effect transistor (MOS FET) located in the liquid-helium bath, and the resulting ac voltage was amplified and detected by a lock-in amplifier. The lock-in output was simultaneously plotted as a function of field on an XY recorder and digitized for later numerical integration. The characteristics of the MOS FET chopper and lock-in amplifier as a dc voltage amplifier compare favorably with the superconducting quantum interference detector (SQUID) preamplifier used previously in the same experimental apparatus.[1] More important, the present system is far more reliable because it is not sensitive to radio-frequency interference as was the SQUID preamp.

Measurements were performed on two samples cut from the same zone-refined niobium single crystal. Sample 1 was spark-machined to a spherical shape, etched, annealed, and surface-oxidized (heated to 400°C in an oxygen atmosphere). The preparation of Sample 2 was identical except that, after spark-machining, it was lapped to a more accurately spherical shape. The results for the two samples were identical except that the transition from the Meissner state to the mixed-intermediate state at H_1 was sharper and the first flux entry into the sample occurred at a slightly higher field in Sample 2. Sample 1 was used for the neutron diffraction measurements of anisotropy effects on the flux line lattice.[2]

Values of the flux density B_0 at H_2, obtained in two ways from the dM/dH measurements, are compared with values obtained from the neutron-diffraction measurements in Fig. 4.10. The essential agreement between the neutron diffraction values of B_0 and those obtained from $M(H_2)$ indicates that the flux line lattice completely fills the sample at H_{c2}. The small discrepancy between these values and the values $B_0 = 3(H_2 - H_1)$ indicates that the first flux entry into the sample occurs not at $^2/_3 H_{c1}$, as expected thermodynamically, but at a slightly higher superheating field.

In Fig. 4.11, magnetization curves for two different sample orientations and the same temperature are

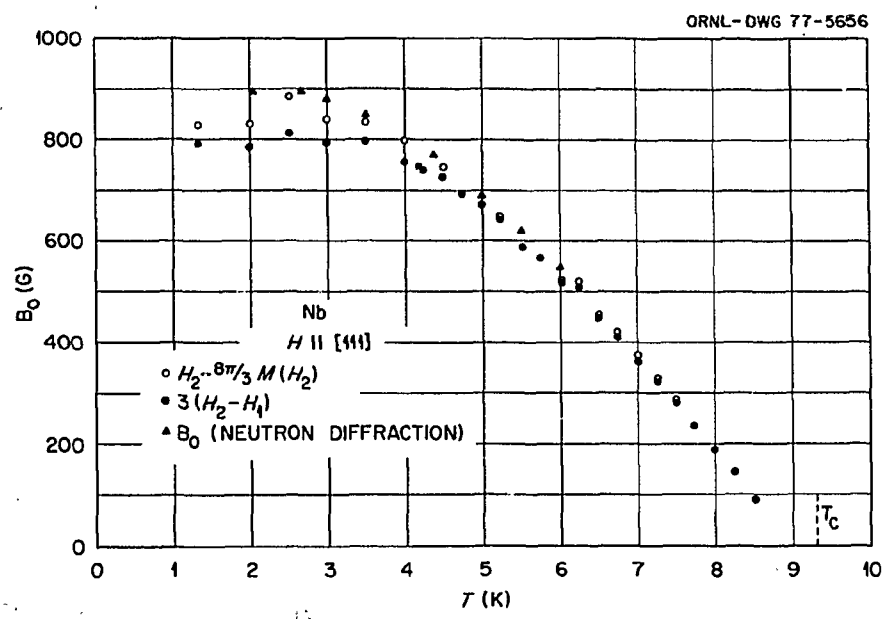

Fig. 4.10. Comparison of three determinations of the equilibrium flux density B_0 at the lower critical field. The measured quantities H_1, H_2, and $M(H_2)$ are discussed in the text.

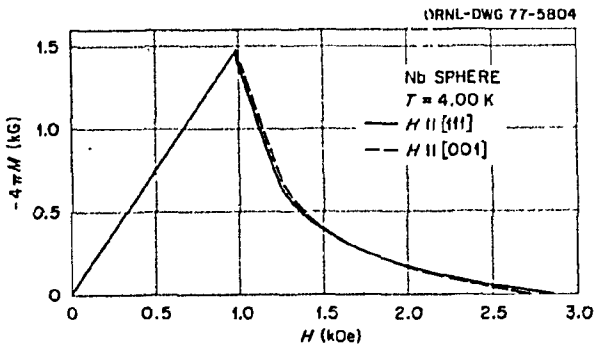

Fig. 4.11. Magnetization curves for a field parallel to two high-symmetry crystalline axes at one temperature.

compared. As is required by thermodynamics, the areas under these curves are the same (experimentally to within 0.5%). Associated with the higher H_{c2} is a smaller slope dM/dH at H_{c2}. In fact, our measurements show that the anisotropy in κ_1 (associated with H_{c2}) is nearly identical to the anisotropy in κ_2 (associated with dM/dH at H_{c2}). The curves cross, and the orientation having the larger H_{c2} has a smaller H_{c1}. There is only a small anisotropy in B_0.

The present study has shown that the neutron diffraction measurements of the area of a unit cell of flux line lattice give the correct average flux density. In addition, these measurements have produced data that were previously unavailable or less reliable, such as $C_L(B_0)$ and the anisotropy of κ_2.

1. H. R. Kerchner and C. C. Watson, *Solid State Div. Annu. Prog. Rep. December 31, 1975*, ORNL-5135, p. 33.
2. D. K. Christen, S. Spooner, and H. R. Kerchner, "Low-Field Anisotropy of the Flux Line Lattice in Superconducting Niobium," this report.

LATTICE DYNAMICS

INVESTIGATION OF THE ANOMALOUS TEMPERATURE DEPENDENCE OF THE SELF-DIFFUSION CONSTANT OF HYDROGEN IN NIOBIUM BY QUASI-ELASTIC NEUTRON SCATTERING[1]

D. Richter[2] A. Heidemann[3]
B. Alefeld[2] N. Wakabayashi

The diffusion constant of hydrogen in niobium was investigated by quasi-elastic neutron scattering in the temperature region 165 to 300 K. By macroscopic methods a transition from a high-temperature activation energy of 106 meV to a low-temperature activation energy of 68 meV was observed in this region. The value of the low-temperature activation energy was confirmed by the neutron scattering experiments. The possibility that the activation energy at low temperature is related to thermally activated tunnelling processes is discussed.

1. Abstract of paper: *J. Phys. F* 7, 569 (1977).
2. Institut für Festkorperforschung, Kernforschungsanlage, Julich, Germany.
3. Institut Laue-Langevin, Grenoble, France.

CHARGE FLUCTUATION MODEL OF LATTICE VIBRATIONS[1]

N. Wakabayashi

A new phenomenological model is proposed for the lattice dynamics of transition metals. It is based on the microscopic model of Sinha and Harmon and includes the effect of charge fluctuations coupled to atomic motions. The model has been found to reproduce very accurately the phonon dispersion curves for niobium with short-range charge fluctuations and interatomic interactions.

1. Abstract of paper: *Solid State Communications* (in press).

LATTICE VIBRATIONS IN ALPHA URANIUM

W. P. Crummett[1] R. M. Nicklow
H. G. Smith N. Wakabayashi

The alpha phase of uranium, stable below 935 K, is orthorhombic with four atoms in the C-centered unit cell. Several low-temperature effects have been observed in α-U including anomalies in the elastic constants,[2,3] specific heat,[4] and lattice parameters.[5] The elastic constant C_{11} is particularly interesting in that it rises to a maximum at 256 K, decreases to a sharp minimum at 43 K (perhaps a discontinuity), and displays hysteresis below this temperature. The net volume thermal expansion is negative below 43 K, and no structural transition is found to occur at this or lower temperatures. All of these anomalies are thought to be electronic in origin. As a superconductor, α-U exhibits additional unusual properties. At zero pressure it is a filamental superconductor with a

T_c above 1 K for polycrystalline samples[6] and less than 0.2 K for single crystals.[7,8] However, bulk superconductivity begins under modest pressure with a maximum T_c of 2.3 K at 11 kbar.[9]

Because the lattice dynamical properties are intimately related to all the properties that show anomalies outlined above, a thorough investigation of the lattice dynamics of α-U, using inelastic neutron scattering techniques, has been undertaken. As an initial step, the room-temperature phonon dispersion curves of a small single crystal[10] (0.106 cm^3) have been measured along the three high-symmetry directions: [ζ00], [0ζ0], and [00ζ]. All the modes in the [00ζ] direction, as well as the acoustic branches in the [0ζ0] direction, show no unusual features. The [0ζ0] optical branches polarized along [100] and [010] are fairly flat, while the [001] polarized optic branch (Δ_3) has some slight dispersion with a broad minimum about $\zeta = 0.8$. The data for the [ζ00] direction are shown in Fig. 4.12. All of these modes are pure at the Brillouin zone center, as are the branches Σ_2 and Σ_3, which have [001] polarization. The other modes correspond to vibrations that may have atomic displacements along both the [100] and [010] directions. At small ζ the Σ_1 acoustic branch is longitudinal-like and is associated with the anomalous elastic constant C_{11}. The slope of the dispersion curve agrees well with that predicted by the room-temperature value of C_{11}. The temperature dependence of the branch in this region has been investigated by Wakabayashi, Nicklow, and Lander.[11] They found that at 300, 50, and 43 K the slope agreed well with the C_{11} values of Fisher and Dever[3] but was somewhat higher than their value at 13.4 K.

A four-neighbor Born–von Kármán model, eight-neighbor axially symmetric model, simple shell model, and a shell model allowing some core-shell overlap were used in attempts to fit the data. All these models fit the [00ζ] data very well and the [0ζ0] data moderately well with the greatest discrepancy appearing in the Δ_3 branch. For the [ζ00] direction the eight-neighbor axially symmetric model reproduced the Σ_2, Σ_3, and Σ_4 branches fairly well. However, none of these models was able to fit the dip in the Σ_1 acoustic curve without introducing dips in the Σ_1 optic branch, which are not seen experimentally.

It appears, therefore, that the room-temperature lattice dynamics of α-U cannot be described by simple phenomenological models. A more sophisticated treatment that includes the effects of the electronic system is probably needed. The investigation is continuing and measurements will be made as a function of temperature and pressure.

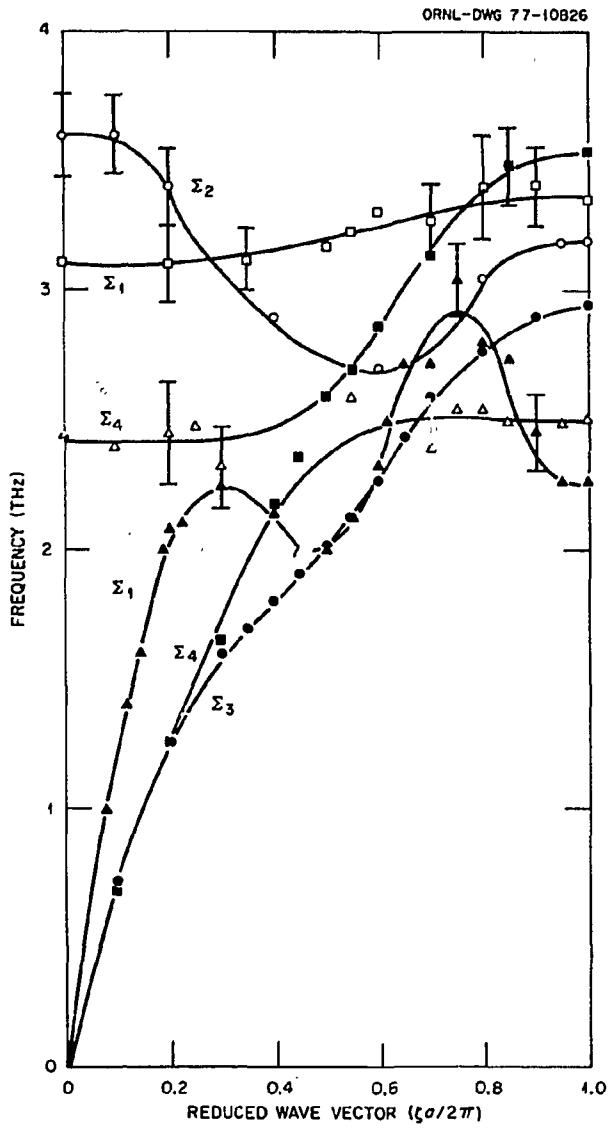

Fig. 4.12. Room temperature phonon dispersion curves for [ζ00] direction of α-U. Unless indicated otherwise uncertainties are less than 5%. Lines are only to guide the eye.

1. ORAU graduate laboratory participant from West Virginia University, Morgantown.

2. H. J. McSkimin and E. S. Fisher, *Phys. Rev.* 31, 1627 (1960).
3. E. S. Fisher and D. Dever, *Phys. Rev.* 170, 607 (1968).
4. J. Crangle and J. Temporal, *J. Phys. F* 3, 1097 (1973).
5. C. S. Barrett, M. H. Mueller, and R. L. Hitterman, *Phys. Rev.* 129, 625 (1963).
6. E. S. Fisher, T. H. Geballe, and J. M. Shreyer, *J. Appl. Phys.* 39, 4478 (1968).

7. T. H. Geballe et al., *Science* 152, 755 (1966).
8. C. Palmy and E. S. Fisher, *Solid State Commun.* 8, 653 (1970).
9. T. F. Smith and E. S. Fisher, *J. Low Temp. Phys.* 12, 631 (1973).
10. The sample was kindly loaned to us by G. Lander and E. S. Fisher at Argonne National Laboratory.
11. N. Wakabayashi, R. M. Nicklow, and G. Lander, private communication.

LATTICE DYNAMICS OF NdSb[1]

N. Wakabayashi A. Furrer[2]

Phonon dispersion curves for NdSb obtained by inelastic neutron scattering techniques have been analyzed on the basis of an axially symmetric force-constant model, a simple shell model, and a screened Coulomb force model. The last model gave the best fit to the experimental data. Various physical properties such as the effective ionic charges, the tetragonal distortion due to the magnetoelastic effect, and the Stark broadening of the transition between the crystal-field levels have been calculated from the model, and the results have been found to be in good agreement with experimental observations.

1. Abstract of paper: *Phys. Rev. B* 13, 4343 (1976).
2. Institut für Reaktortechnik ETHZ, Würenlingen, Switzerland.

LATTICE DYNAMICS OF LAYERED STRUCTURES[1]

N. Wakabayashi

The lattice dynamics of layered compounds is discussed on the basis of a set of two-dimensional lattices perturbed by weak interlayer interactions. Experimental observations that indicate quasi two-dimensional character such as the temperature dependence of Debye temperatures and Kohn anomalies are emphasized.

1. Abstract of paper: *Nuovo Cimento* 38, 256 (1977).

LATTICE DYNAMICS OF Ni_xPt_{1-x}

N. Kunitomi[1] N. Wakabayashi
Y. Tsunoda[1] R. M. Nicklow
H. G. Smith

The alloy system Ni_xPt_{1-x} forms a solid solution in the entire range of concentration, x. Phonon dispersion curves for pure nickel and platinum are very similar, but the frequencies do not scale as the ratio of the square root of the atomic masses. This indicates that, although these elements have the same valence, the interatomic forces differ considerably. To investigate the validity of existing theories of phonons in disordered systems, detailed measurements of the double-differential neutron scattering cross section due to lattice vibrations have been performed on this alloy system for $x = 0.05$, 0.25, 0.50, 0.70, and 0.95. Peak positions in the scattered neutron groups for wave vectors in the [001] direction are plotted in Fig. 4.13. For $x = 0.95$, the double peak features expected for resonance modes are observed near 3.3 THz, both for longitudinal and transverse branches. However, as the platinum concentration is increased, the observed perturbations on these two branches become different. In the coherent potential approximation, such an effect requires the existence of a branch-dependent self-

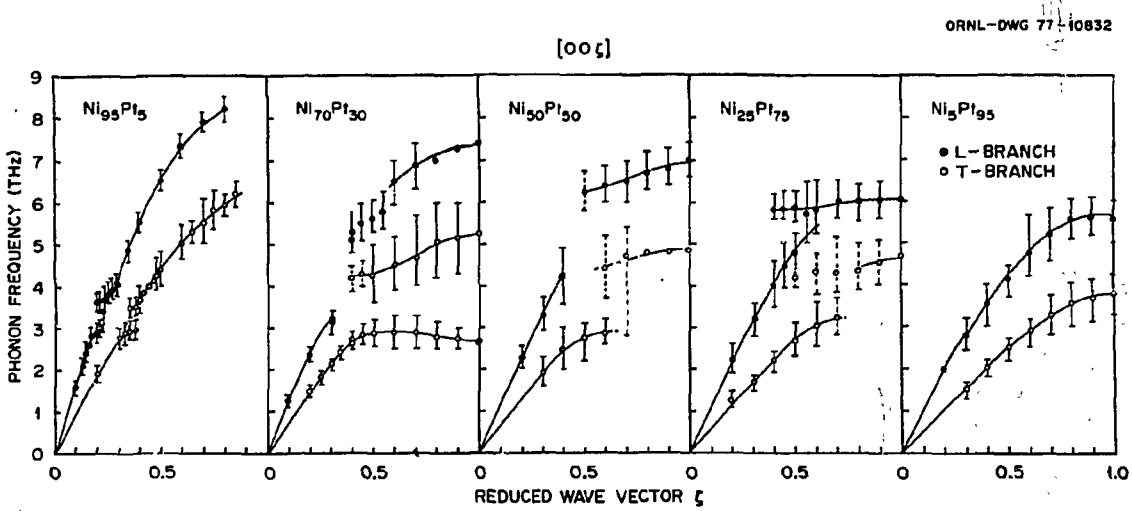

Fig. 4.13. Phonon dispersion curves for Ni-Pt alloys in the [001] direction. Open (filled) circles represent peak positions in the scattered neutron groups for the transverse (longitudinal) branch.

energy. This, in turn, indicates the importance of the changes in the interatomic forces in these alloys. No local mode separated from the band modes could be observed for $x = 0.05$ contrary to the prediction of a mass-defect theory. This also shows a significant change in the interatomic forces. The CPA-F theory of Mostoller and Kaplan may be adequate in qualitatively reproducing the data. Attempts will be made in the future to construct a model that is in quantitative agreement with the data.

1. Guest scientist from Osaka University, Toyonaka, Japan.

PHONONS AND PHASE TRANSITION IN 1T-$TiSe_2$

N. Wakabayashi K. C. Woo[1]
H. G. Smith F. C. Brown[1]

It was demonstrated by electron and x-ray diffraction[2] that in the layered compound 1T-$TiSe_2$ a superlattice forms below approximately 200 K with new lattice parameters twice as large as those of the high-temperature phase. It was also established by neutron diffraction[3] that the superlattice reflection appears at the L point, that is, $q = (1/2, 0, 1/2)$, and that the atomic displacements are transverse and are parallel to the plane of the layers involving both titanium and selenium atoms. The transition has been interpreted to be driven by an electron-electron or an electron-hole coupling near the Fermi surface.

To obtain information about the dynamics of this transition and also about the phonon dispersion curves in general, inelastic neutron scattering measurements have been carried out on a small single crystal at various temperatures. Measurements were performed for wave vectors $(\zeta 00)$ and $(\zeta 0 1/2)$ with $\zeta = 0 \sim 1/2$. Figure 4.14 shows the dispersion curves measured in the [100] direction for branches with polarization vectors confined in the $(\bar{2}10)$ plane, that is, those having no transverse components parallel to the plane of the layers. An upward curvature exists near $q = 0$ in the transverse-like acoustic branch as expected for a layered compound, but no unusual features have been observed in these branches. The set of data shown in the figure is a compilation of measurements both at room temperature (open symbols) and 20 K (filled symbols) and do not show significant differences at these temperatures. Also the transverse acoustic mode measured at room temperature (Fig. 4.15*a*) does not show anomalies. Measurements for $(\zeta 0 1/2)$ have been considerably more difficult because of lower scattering intensities. However, in the scattered neutron groups, there are peaks that indicate the existence of a low-frequency transverse branch (Fig. 4.15*b*). Furthermore, the peak corresponding to the phonon at L (denoted by the arrow in Fig. 4.15*b*) has a temperature dependence shown in Fig. 4.15*c*. Although peaks seem to exist both above and below the transition temperature (about 200 K), no well-defined peak could be observed at 180 K. Also no significant temperature effect could be detected in other modes. This may be interpreted as a soft mode behavior associated with the phase transition.

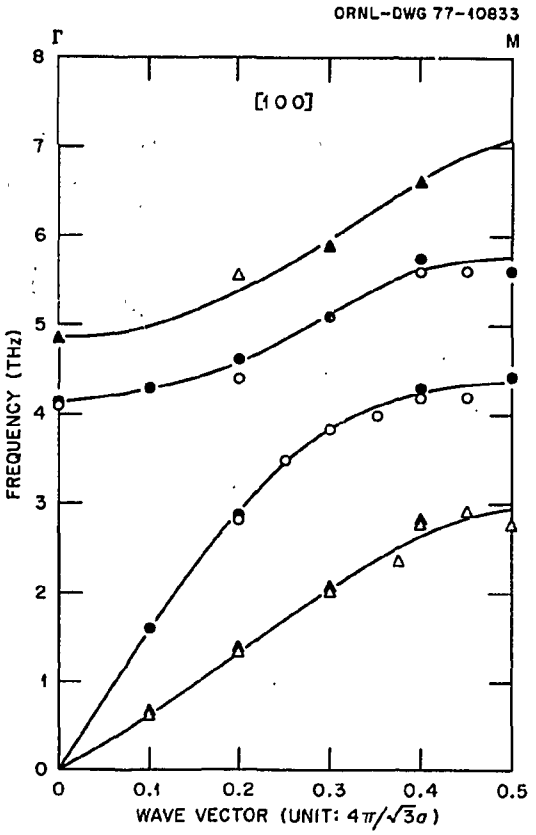

Fig. 4.14. Phonon dispersion curves for $TiSe_2$ in the [100] direction. The data shown are for those modes having no transverse component parallel to the plane of the layers. The lines are merely a guide to the eye.

The solid lines in Fig. 4.15*a* and *b* represent the frequencies calculated on the basis of a simple force constant model. The model reproduces the experimental data rather well; and for a set of different values of force constants, it produces a softening of a transverse mode at L without altering other branches beyond experimental uncertainties. The dashed lines

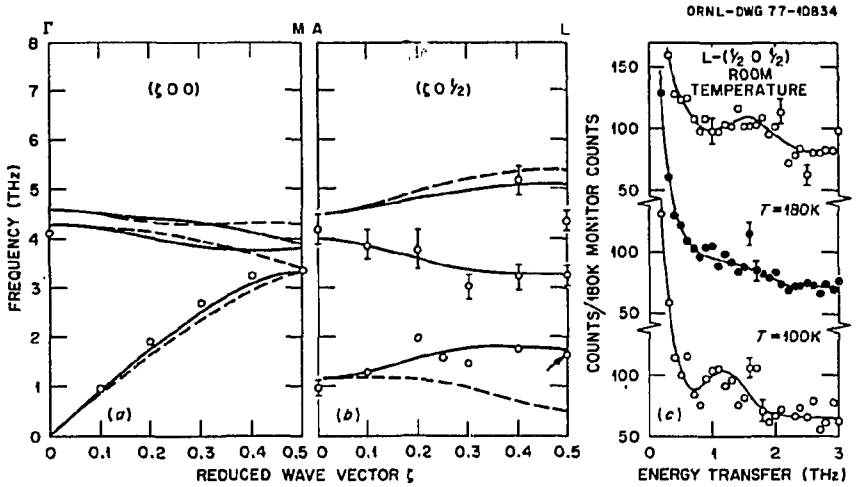

Fig. 4.15. Transverse phonons measured for $TiSe_2$. (*a*) Transverse phonons for (ζ00) at room temperature. The lines represent the results of the model calculations. (*b*) Transverse phonons ($\zeta 0 \frac{1}{2}$) at room temperature. (*c*) Scattered neutron groups at *L* corresponding to the mode denoted by the arrow in (*b*). The lines are merely a guide to the eye.

in the figure have been calculated with the values for *interlayer* interactions different from those used in the calculation for the solid lines. The soft phonon in this model involves motions of both titanium and selenium atoms in agreement with the conclusion of the neutron diffraction study. Thus the bonding between the selenium atoms in the neighboring layers seems to be responsible for the phase transition. However, the relationship between the description of the transition in terms of such a force model and that in terms of an electronically driven lattice instability is not understood at present.

1. University of Illinois, Urbana.
2. K. C. Wood et al., *Phys. Rev. B* 14, 3242 (1976).
3. F. J. DiSalvo, D. E. Moncton, and J. V. Waszczak, *Phys. Rev. B* 14, 432 (1976).

PHONON ANOMALIES IN TRANSITION METALS, ALLOYS, AND COMPOUNDS[1]

H. G. Smith N. Wakabayashi
Mark Mostoller

The anomalous features observed in the dispersion curves of several *d*-band superconducting materials are reviewed, and comparisons are made with related nonsuperconducting materials. The results are briefly discussed in terms of some theoretical models. New neutron scattering data are presented for niobium with oxygen impurities, the Mo-Re bcc alloy system, and the hcp metals technetium and ruthenium.

1. Abstract of paper: p. 233 in *Superconductivity in d- and f-Band Metals*, ed. by D. H. Douglass, Plenum Press, New York, 1976.

PHONON LINE WIDTHS IN NIOBIUM

H. G. Smith N. Wakabayashi
W. H. Butler[1]

The electron-phonon coupling constant, λ, of a superconductor has been defined by McMillan in terms of the spectral function $\alpha^2(\omega)F(\omega)$, which can be obtained directly from tunneling measurements. The phonon density of states, $F(\omega)$, is obtainable from neutron scattering measurements. Allen[2] has shown that $\alpha^2 F$ can be related to the electron-phonon contribution to the phonon line widths $\gamma_i(q)$ throughout the Brillouin zone by

$$\alpha^2 F = 2/\pi \; N(0)\omega \sum_{q,i} \gamma_i(q)\delta(\omega - \omega_q) \; ,$$

where $N(0)$ is the electronic density of states at the Fermi energy. It would be a formidable task to determine this quantity by measuring a sufficient number of phonon line widths. Allen introduced an

average phonon width, $\bar{\gamma}$, which is related to the McMillan parameter, λ, by

$$\bar{\gamma}/\bar{\omega} = \frac{\pi}{12}(\lambda\bar{\omega}/W) ,$$

where $\bar{\omega}$ is defined as $\langle\omega^2\rangle^{1/2}$ and W is an effective bandwidth defined by $N(0) = N/W$; N is the number of atoms in the crystal. In general, this quantity is expected to be very small and perhaps experimentally inaccessible except for materials with large electron-phonon interactions, such as the A-15 compounds. This has been confirmed by Axe and Shirane[3] in their studies of phonon line widths in Nb_3Sn above and below the superconducting transition temperature for phonon energies of the order of $2\Delta(T)$, the superconducting energy gap. Very careful work by Shapiro et al.[4] also detected changes in phonon line widths in niobium above and below T_c, even though the average line widths were much less than in Nb_3Sn.

Allen[2] also showed how the electron-phonon line widths are related to the screened electron-phonon matrix elements. The calculation of the line widths from this relation requires an accurate knowledge of the band structure and the wave functions at the Fermi surface. These quantities have been calculated for niobium by Butler and Allen[5] using first principles KKR wave functions and the muffin tin approximation. Calculated throughout the Brillouin zone, the line widths reveal a very large dispersion of $\gamma_i(q)$ as a function of q, i; for large q, $\gamma(q)$ is more than an order of magnitude larger than for small values of q where the phonon energies are of the order of the energy gap. Because the anomalous dispersion relation in niobium is believed to be related to the electron-phonon interaction, one would expect that the largest widths would coincide with the largest anomalous dips observed in the phonon dispersion curves, but this does not seem to be the case. However, as discussed below, large anomalies may not necessarily be in the form of a dip.

A preliminary inelastic neutron scattering investigation of the phonon line widths in a large single crystal of niobium has been made at about 13 K. The crystal was rotated about the $[1\bar{1}0]$ axis, and phonons were measured in the high symmetry [001], [110], and [111] directions under conditions of relatively high energy and momentum resolution. The theoretical calculations predicted that the phonon line widths would be much larger for the [110] LA phonons with a maximum width near the point N; therefore, the major part of this study has been concentrated on measuring phonon line widths of longitudinal and transverse phonons in this direction. For completeness several TA and LA phonons were measured in the [100] and [111] directions. Generally, the dominant contribution to the width of a phonon group is due to the instrumental resolution. For this experiment the resolution function was measured, and the instrumental contribution to the line width was calculated for each of the phonons measured. A knowledge of the slope of the dispersion curves is also required for the calculation, and the slopes were obtained from the room-temperature phonon measurements of Nakagawa and Woods.[6] The slopes of the dispersion curves obtained at 13 K are preferred, but they are not available at this time.

As can be seen in Fig. 4.16, the measurements of the widths of the LA [110] phonons dramatically confirm the theoretical predictions of Butler and Allen.[5] The experimental phonon widths have been deduced from the total measured line widths with the aid of the experimental resolution function of the triple-axis spectrometer. Actually, these widths contain certain other contributions due to anharmonicity, etc., but several phonon measurements at room temperature suggest that these contributions are small.

The theoretical prediction and experimental confirmation of strong electron-phonon coupling because of phonons in this region of the Brillouin zone are very interesting. This particular region is not usually considered to be anomalous; however, an examination of the phonon curves for Nb-Mo alloys[7] shows that the longitudinal phonon frequencies along [110] for $\zeta < 0.3$ are strongly depressed in niobium relative to a $Nb_{0.25}Mo_{0.75}$ alloy. It is probable that addition of molybdenum to niobium decreases the electron-phonon interaction because of the reduction in $N(0)$ and allows the observed frequencies to rise toward their bare unscreened values. In fact, the longitudinal phonon frequencies near the N point change fastest of all on addition of molybdenum to niobium.

The phonon line width measurements in the [100] and [111] directions are currently being analyzed and deconvoluted and will be included in a full report of this investigation.

---

1. Metals and Ceramics Division, ORNL.
2. P. B. Allen, *Phys. Rev. B* **6**, 2577 (1972).
3. J. D. Axe and G. Shirane, *Phys. Rev. Lett.* **30**, 214 (1973).
4. S. M. Shapiro, G. Shirane, and J. D. Axe, *Phys. Rev. B* **12**, 4899 (1975).
5. W. H. Butler and P. B. Allen, *Bull. Am. Phys. Soc.* **22**, 263 (1977).

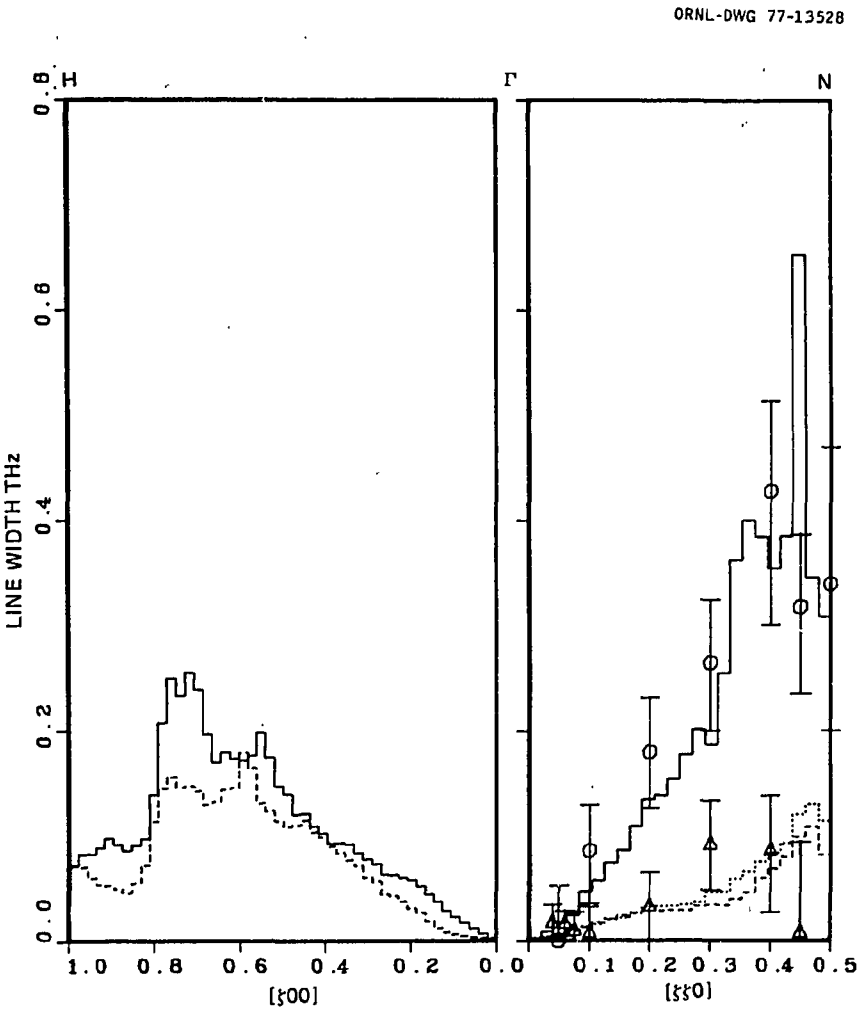

Fig. 4.16. Phonon line widths (FWHM) vs wave vector in niobium at 13 K. The solid (dashed) curves represent the calculated electron-phonon contributions to the line widths for the longitudinal (transverse) branches. The circles (triangles) are the experimentally determined electron-phonon line widths for the longitudinal (transverse) branches. The vertical lines represent the estimated uncertainties.

6. Y. Nakagawa and A.D.B. Woods, p. 39 in *Proceedings of the International Conference on Lattice Dynamics*, ed. by R. F. Wallis, Pergamon, New York, 1963.

7. B. M. Powell, P. Martel, and A.D.B. Woods, *Phys. Rev.* **171**, 727 (1968).

INVESTIGATIONS OF PHONON PERTURBATIONS BY DEFECTS[1]

R. M. Nicklow

Recent experimental investigations of phonon perturbations by defects will be reviewed. Emphasis will be on (1) the study of complex defects, such as the split-interstitials occurring in irradiated metals and (perhaps) in ionic-conducting silver halides, and (2) the molecular substitutional defect CN^- in KCl.

1. Abstract of paper: p. 117 in *Proceedings of the Conference on Neutron Scattering*, vol. I, ed. by R. M. Moon, ERDA CONF-760601-P1, Oak Ridge, Tenn., 1976.

LATTICE DYNAMICS OF β-SILVER IODIDE

W. Bührer[1] R. M. Nicklow
P. Brüesch[2]

The migration of silver through AgI has found wide technical application for many years in

photographic processes and, more recently, in solid state batteries in which AgI and AgI-based compounds serve as solid electrolytes. Because the diffusion of ions through crystals is a thermally activated process, ionic conductivity is closely related to the phonon spectrum, and a knowledge of the lattice vibrations is therefore important for the understanding of the observed phenomena. Consequently we have carried out neutron inelastic scattering measurements of the phonon dispersion relation along the Σ, T, and Δ symmetry directions in hexagonal β-AgI. The initial measurements were carried out at room temperature at the Diorit reactor in Würenlingen, Switzerland.[3] These measurements were extended, and measurements at several temperatures between 80 K and room temperature were carried out on a triple-axis spectrometer at the High Flux Isotope Reactor (HFIR).

To date, fairly complete results have been obtained at 160 K (Fig. 4.17). The lines shown are only guides for the eye and do not represent theoretical results. Because of strong anharmonicity and mode interaction effects, it has proved difficult to obtain a complete mapping of the entire dispersion relation. Additional measurements will be obtained in the near future. A rather striking feature of the results is the very low frequency of certain optic modes, for example, Δ_4, T_2, and Σ_2. These modes may be indirectly related to the β-α crystal structure transition at 420 K; however, their temperature dependence between 80 and 300 K is quite small.

The data have been analyzed with a "valence shell model": valence forces were used to describe the short-range forces, and a shell model was used for the ionic polarizabilities and the long-range Coulomb interactions. The agreement with the data is fairly good with the exception of the longitudinal acoustic modes, which are calculated to have lower frequencies than those observed. The model has been used to calculate several phonon-related properties of AgI. One property that is related to ionic conductivity is the mean square vibrational amplitude of the ions. Good agreement is obtained between the calculated and measured amplitudes[4] (Fig. 4.18).

1. Institute für Reaktorforschung, Würenlingen, Switzerland.
2. Brown Boveri Research Center, Baden, Switzerland.

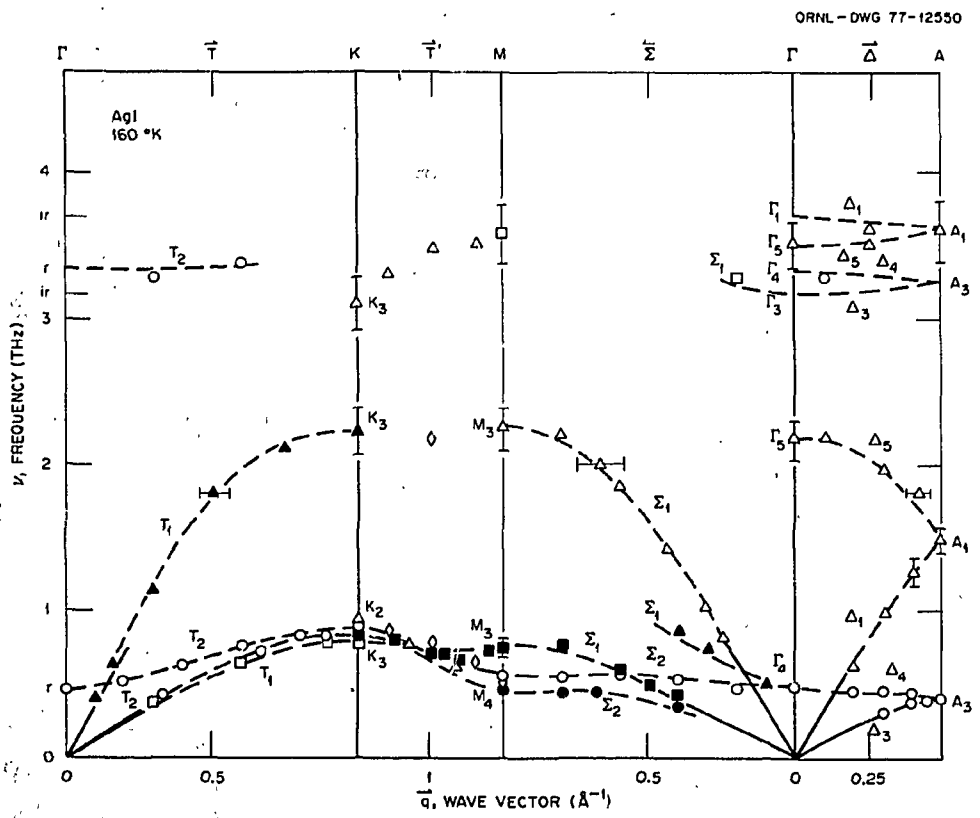

Fig. 4.17. Phonon dispersion curves of β-AgI at 160 K.

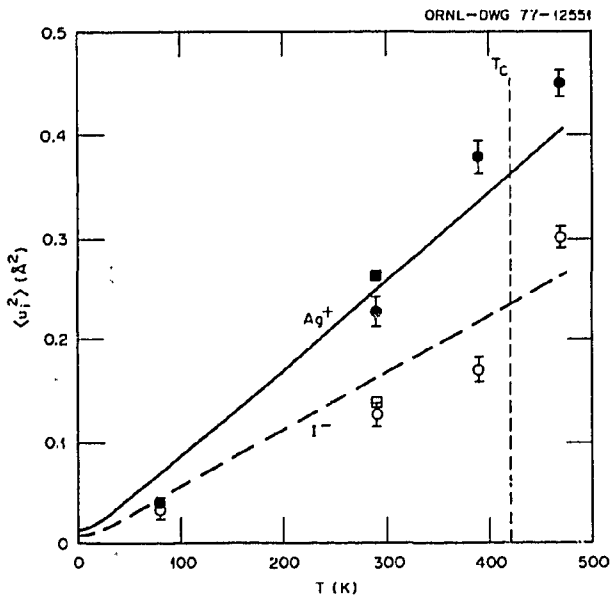

Fig. 4.18. Mean square displacements for Ag^+ and I^- in β-AgI. The lines (solid, Ag^+; dashed, I^-) are calculated with the force model obtained from the dispersion curve measurements. The open and closed circles are experimental points for iodine and silver from neutron scattering data. The corresponding squares are from x-ray data.

3. W. Bührer and P. Brüesch, *Solid State Commun.* **16**, 155 (1975).

4. G. Burley, *J. Chem. Phys.* 38, 2807 (1963), and W. Bührer, *Neutron Scattering Progress Report*, AF-SSP-74, Würenlingen (1974).

THE TEMPERATURE DEPENDENCE OF PHONON-DEFECT MODE HYBRIDIZATION IN KCl:CN

R. M. Nicklow

The CN^- radical, when placed in the alkali halides as a substitutional impurity, is a complex defect which exhibits a wide variety of motions including tunneling, libration, and free rotation.[1] In KCl the potential barrier between equivalent CN^- ⟨111⟩ orientations is believed to be 4 to 5 meV. The lowest energy levels for CN^- in KCl consist of a ground state that is split by tunneling into four levels separated by about 0.15 meV.[2,3] Above these tunneling states several groups of librational levels are centered at approximately 1.6, 2, and 4 meV. Higher levels presumably correspond to hindered rotations and free rotations.

Phonons can interact with these highly anharmonic molecular motions if the matrix element $\langle e|x|g\rangle$ of a displacement coordinate x between a defect state $|g\rangle$ and another state $|e\rangle$ is finite. Theoretical studies of a two-level defect show that the strength of the interaction also depends on the relative thermal population of the two energy states,[4,5] which leads to a temperature dependence of the corresponding phonon perturbation.

Previously we observed, for KCl containing about 0.4% CN^- impurities, a strong perturbation of the [110] transverse phonon branch (with $[1\bar{1}0]$ polarization) at 5 K.[6] The energy of the phonons that are perturbed most is approximately 0.5 THz (about 2 meV), corresponding quite well with the transition energy from the ground states to the CN^- librational levels. To investigate the temperature dependence of these phonon-defect interactions, we have measured the [110] transverse branch between 10 and 120 K. Ultrasonic measurements indicate that the defect-induced changes in the velocity of sound appropriate to this branch are strongly temperature dependent above 10 K, nearly vanishing by 50 K.[7] A similar result is observed in our neutron scattering measurements (Figs. 4.19 and 4.20).

At 120 K the dispersion curve for KCl:CN for $\zeta \gtrsim 0.13$ and $\nu \gtrsim 1.0$ THz agrees very well with that measured for pure KCl, which is represented by the dotted line in Fig. 4.19. For lower frequencies a small difference exists between the results for pure KCl and

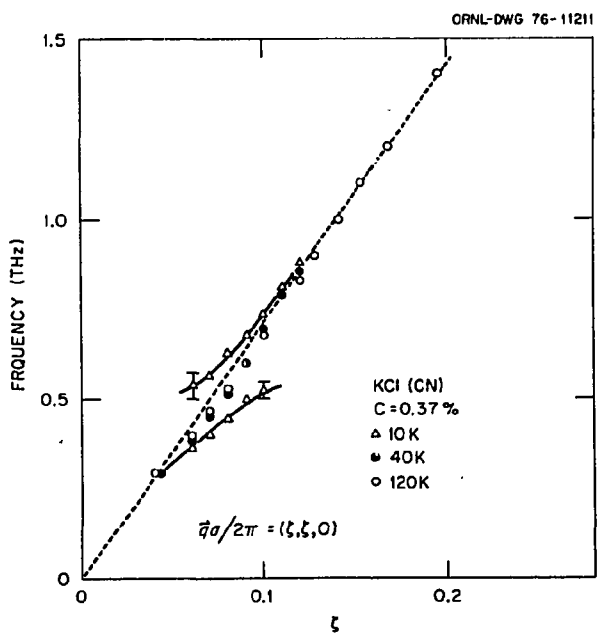

Fig. 4.19. Dispersion relation for coupled defect-phonon modes in $KCl_{1-c}(CN)_c$ for $c = 0.0037$ at different temperatures. The dotted line is the dispersion relation for pure KCl.

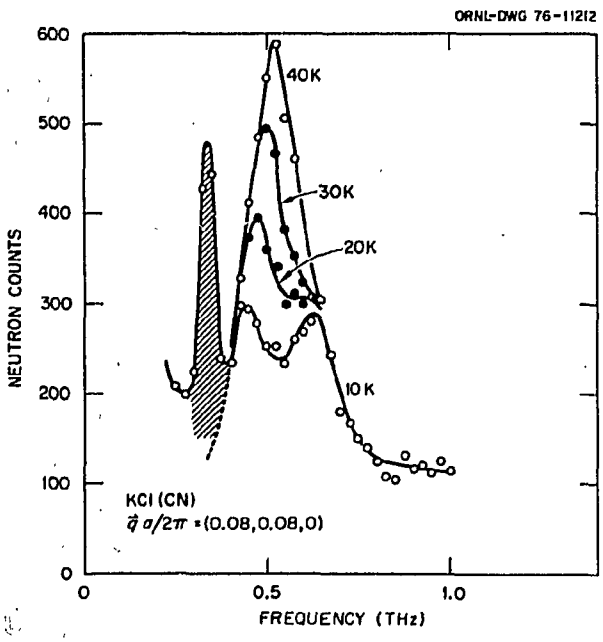

Fig. 4.20. Temperature dependence of the frequency distribution of neutrons scattered from KCl(CN) for q = (1.92, 2.08, 0)$2\pi/a$. The shaded peak is Bragg-scattering contamination.

KCl:CN, which may be due to weak phonon coupling to the molecular transitions to the highest (4 meV) librational levels. A more striking phonon perturbation occurs because of coupling to the lower librational levels, as is illustrated in Fig. 4.20 for $\zeta = 0.08$. As the temperature is reduced below 40 K, the single phonon peak in a constant-Q neutron scan gradually develops significant structure, becoming two peaks of nearly equal intensity at 10 K. The resulting hybridization-split dispersion relation at 10 K is illustrated (Fig. 4.19). Such measurements, together with observations of the magnitude of the defect-phonon coupling for phonons of various symmetries and their comparisons with theoretical calculations of the matrix elements $\langle e|x|g\rangle$, should provide sufficient information to allow a determination of defect-host interactions and consequently the molecular energy states and wave functions.

1. V. Narayanamurti and R. O. Pohl, *Rev. Mod. Phys.* 42, 201 (1970).
2. Fritz Lüty, *Phys. Rev. B* 10, 3677 (1974).
3. Hans U. Beyeler, *Phys. Rev. B* 11, 3078 (1975).
4. M. V. Klein, *Phys. Rev.* 186, 839 (1969).
5. D. Walton, *Phys. Rev. B* 7, 3925 (1973).
6. D. Walton, H. A. Mook, and R. M. Nicklow, *Phys. Rev. Lett.* 33, 412 (1974).
7. N. E. Byer and H. S. Sack, *Phys. Status Solidi* 30, 569 (1968).

MEASUREMENT OF DISPERSION CURVES ON ALUMINUM REACTOR-IRRADIATED AT 4.6 K

K. Böning[1] H. J. Fenzl[2]
G. S. Bauer[2] R. Scherm[3]
R. M. Nicklow

The self-interstitials produced in aluminum by low-temperature irradiation with fast particles have [100] dumbbell configurations. They have been predicted[4] to perform low-frequency resonant vibrations that should have a pronounced effect on the transverse [ζ00] phonon dispersion curve: a resonant perturbation at $\zeta \approx 0.15$ ($\nu \approx 1.3$ THz) together with a change of the initial slope. In a previous experiment[5] performed at Institut Laue-Langevin with an aluminum sample neutron-irradiated to about 810 ppm Frenkel defects, we were able to confirm the change of slope in essential agreement with the value expected from the change of the elastic constants of electron-irradiated aluminum.[6] However, no resonance-like behavior was observed in the range $0.05 \leqslant \zeta \leqslant 0.19$.

The new experiment was performed to check the older results using a different aluminum sample with different Frenkel defect concentration (510 ppm) and to extend the ζ range to higher values. With $\mathbf{Q} = (2, \zeta, 0)\cdot 2\pi/a$, the typical line widths were $\Gamma = 0.08$–0.11 THz in the range $0.07 < \zeta < 0.40$. The line positions ν were obtained by fitting the data to Gaussian peak shapes.

As a consequence of the large line width, it was not possible to draw any conclusions on possible line-splitting from the shapes of the measured phonon lines. The measured frequency shifts observed for the irradiated samples relative to the dispersion curve after room-temperature annealing indicate that the change in slope found earlier[6] has been confirmed also for this defect concentration. No significant indication for a resonance-like behavior in the frequency shifts is observed in the new experiment.

1. Technischen Universität München, Garching, Germany.
2. Institut für Festkorperförschung, Kernforschungsanlage, Jülich, Germany.
3. Institut Laue-Langevin, Grenoble, France.

4. H. R. Schober, V. K. Tewary, and P. H. Dederichs, *Z. Phys.* B21, 255 (1975).
5. *Institut Laue-Langevin Annual Report 1976*, Exp. No. 07-05-003 A.
6. K. Böning et al., *Physical Review Letters* (in press).

NEUTRON INELASTIC SCATTERING STUDY OF TETRATHIAFULVALENE-TETRACYANOQUINODIMETHANE (TTF-TCNQ)[1]

H. A. Mook Charles R. Watson, Jr.[2]

Neutron inelastic scattering techniques have been used to measure the phonon dispersion curves along the chain direction in TTF-TCNQ. Most of the branches are rather flat and probably stem from excitations within the TTF or TCNQ molecules. Longitudinal and transverse acoustic modes were also measured, and a large Kohn anomaly that seems to stem from the longitudinal branch was observed at 0.295 $(2\pi/b)$.

1. Abstract of paper: *Phys. Rev. Lett.* 36, 801 (1976).
2. Chemistry Division, ORNL.

A REEXAMINATION OF THE INELASTIC NEUTRON SCATTERING IN TETRATHIAFULVALENE-TETRACYANOQUINODIMETHANE (TTF-TCNQ)[1]

H. A. Mook G. Shirane[2]
S. M. Shapiro[2]

Neutron inelastic scattering measurements have been repeated on deuterated and protonated TTF-TCNQ samples at BNL and ORNL to clarify the phonon scattering and the scattering found at $q = 2k_F$. Good agreement is found between the phonon measurements made in the two laboratories on both samples. Differences in the slope of the transverse acoustic phonon originally reported between the two laboratories can most likely be ascribed to the wider mosaic spread of the ORNL sample. Measurements at $q = 2k_F$ at room temperature are presented, and no distinct anomaly is observed for an energy transfer of 3.3 meV. From this we estimate that any scattering at $2k_F$ at room temperature must be smaller than about 8% of the LA phonon intensity for 2.9 meV.

1. Abstract of paper to be published.
2. Brookhaven National Laboratory, Upton, Long Island, New York.

PHONONS IN THE MIXED VALENCE SYSTEM $Sm_{0.75}Y_{0.25}S$

H. A. Mook T. Penney[1]

Under modest pressures SmS changes in volume by around 15% and goes from an insulating black phase to a metallic gold phase. This lattice collapse is thought to result from a change in the configuration of the samarium ion from a divalent f^6 state to a trivalent f^5d configuration. The lattice constants of trivalent samarium salts are much smaller than those of the divalent salts. In a free ion the f^5d state is 2 to 3 eV above the f^6, but in a crystalline field the lowest f^5d (t_{2g}) state is nearly degenerate with the f^6. If the density of the d levels is of the order of 1 state/eV·atom, a large fraction of an electron per ion could leave the f^6 configuration and occupy the f^5d. Similar effects can be produced at atmospheric pressure in some alloys; YS has a sufficiently small lattice parameter that alloying it into SmS produces a strain similar to applying pressure. If one is near the composition in which 20% of SmS is replaced by YS, a phase transition takes place as one cools from room temperature such that the material expands suddenly and changes from gold to black. We chose a composition with slightly excess YS so that the phase transition is smoothed out over 100 K or so in hopes that the crystals would not break in cooling. Grown at the IBM Research Laboratory at Yorktown Heights, the samples consisted of several crystals about 0.2 cm in size.

Neutrons turn out to be a particularly sensitive probe of the mixed valence system because the energy widths involved in the mixed valence states are comparable to or slightly larger than the energy resolution available on standard neutron spectrometers. X-ray photoemission reveals two spectra characteristic of Sm^{2+} and Sm^{3+} configurations for the SmS/YS mixed valence systems, showing that two configurations are present, but does not distinguish between a homogeneous and inhomogeneous mixed valence state.[2-3] The resolution of the x-ray photoemission experiments gives it a sampling time scale of around 10^{-15} sec so that any fluctuations between the configurations must be slow compared to this time. Mössbauer isomer shift measurements show a well-defined line at energies intermediate between the characteristic energies of the two valence states.[4] The Mössbauer measurements have a time scale of about 10^{-9} sec so that valence fluctuations must be faster than this time. The Mössbauer

measurements also show that the mixed valence compounds are homogeneously of mixed valence.

Neutron energy resolutions are about 1 meV corresponding to fluctuation times of around 10^{-13} sec and thus are in the interesting range between the x-ray and Mössbauer experiments. It turns out this is the time scale of importance in the mixed valence systems.

Phonons have a frequency of about 10^{12} THz and thus may be expected to couple to the volume change effects produced by the fluctuating valence system. Velocity of sound measurements show that certain combinations of elastic constants have discontinuities at the Sm^{2+} to Sm^{3+} transition in the $Sm_{0.75}Y_{0.25}S$ system, and one finds the bulk modulus given by the combination of elastic constants $(c_{11}+2c_{12})/3$ goes to zero at the transition. This combination of elastic constants is an eigenvalue of the elastic constant matrix corresponding to the A_1 irreducible representation that has the full cubic symmetry. The introduction of a wave vector into the system breaks some symmetry elements so that an acoustic wave cannot have complete A_1 symmetry. We thus do not expect to have a soft phonon at the phase transition in the usual sense but expect the mixed valence effects to show up in all the phonon modes that change the volume of the unit cell.

Figure 4.21 shows the phonon modes measured at room temperature when the $Sm_{0.75}Y_{0.25}S$ is in the gold phase where lattice constant extrapolations suggest that the configuration is 30% Sm^{2+} and 70% Sm^{3+}. Thus, while the material is gold in color, we still are in a mixed valence situation; this is reflected by the phonon spectra. Phonon measurements on SmS that has a single valence showed rather standard phonon dispersion curves.[5] Our measurements of the mixed valence system have a number of unusual features. One finds that the LA phonons are unusually low in energy compared to the TA modes, and in the (111) direction the LA mode is below the TA mode. The LA modes are also very broad in energy while the TA modes are quite sharp. The width of the bar associated with each point represents its full width at half height. One might expect the (111) direction to be most sensitive to mixed valence effects because SmS has the rock salt structure in which alternating planes of samarium and sulfur atoms exist along the (111) direction. The LA phonons are the ones that vary the distance between the ions so that one would expect them to be sensitive to the volume fluctuations of the mixed valence state. The TA phonon vibrations are transverse to the spacing between the ions and are not particularly sensitive to fluctuations in the distance between the atoms. Figure 4.21 shows that the LO phonons are also soft, falling below the TO phonons, and are very broad in energy. The TO phonons also appear to be broad in energy, and the optical phonons in general are not well defined. A flat mode

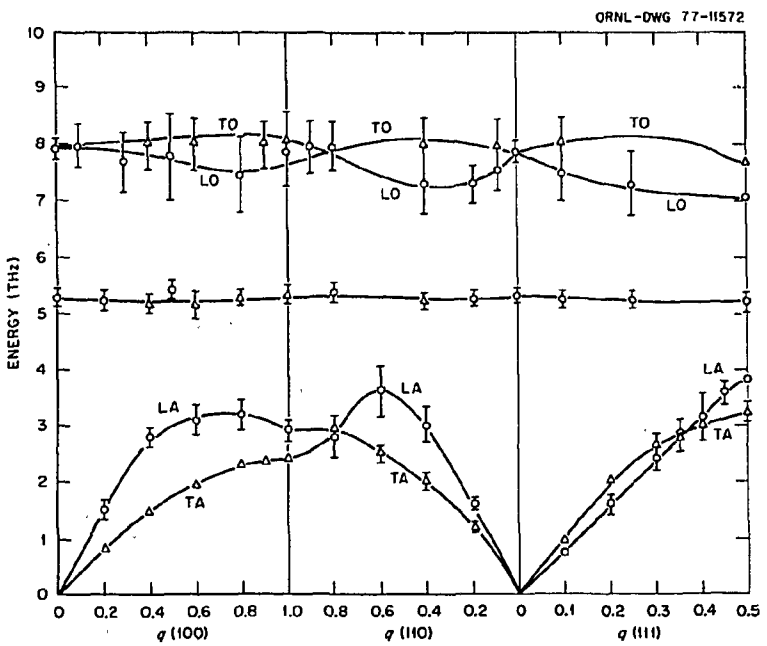

Fig. 4.21. Phonons in $Sm_{0.75}Y_{0.25}S$ measured at 293 K.

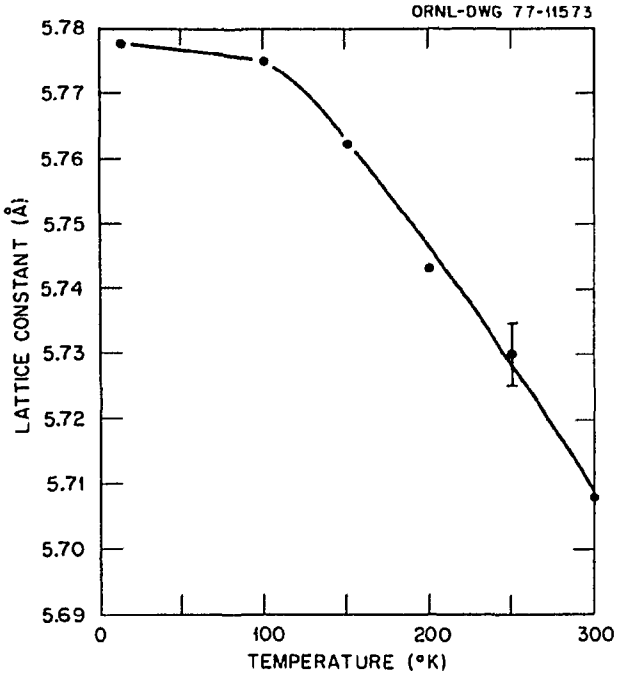

Fig. 4.22. Lattice constant of $Sm_{0.75}Y_{0.25}S$ measured as a function of temperature.

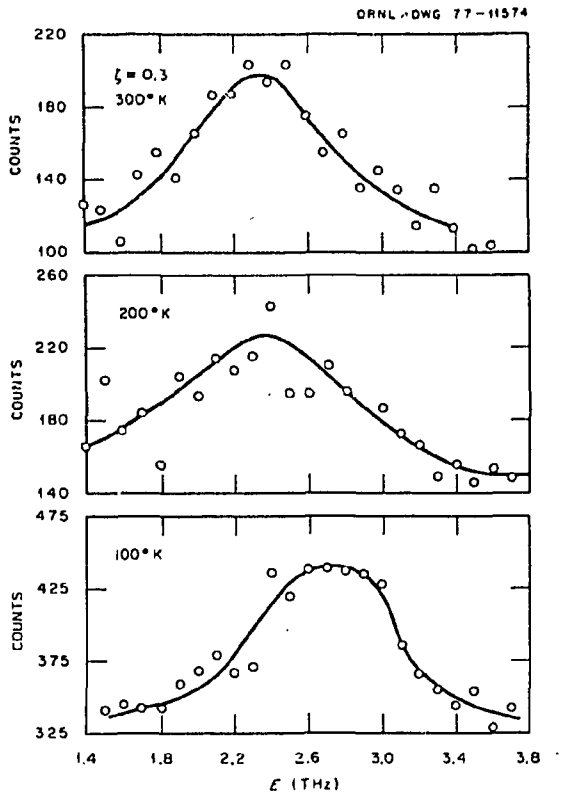

Fig. 4.23. Phonon measurements in $Sm_{0.75}Y_{0.25}S$ at 0.3 of the zone boundary in the (111) direction for 100 K, 200 K, and 293 K.

that appears between the acoustical and optical modes seems to be a local mode stemming from the yttrium, which is considerably lighter than the samarium.

As the $Sm_{0.75}Y_{0.25}S$ is cooled to lower temperature, the lattice constant expands. Figure 4.22 shows a graph of the lattice constant vs temperature. Using a lattice constant extrapolation, we find that at 200 K the valence is about 55% Sm^{2+} and at 100 K about 75% Sm^{2+}. We have chosen to examine the phonons along the (111) direction in detail as a function of temperature. Measurements have been made at room temperature, 200 K, and 100 K. Figure 4.23 shows an LA phonon measurement at $\zeta = 0.3$, which is 60% of the way to the zone boundary for the (111) direction. At room temperature, one sees a broad peak at about 2.4 THz with a tail extending to higher energies. The arrow shows the position of the phonon in the black SmS single valence system. As one cools to 200 K, where the material is about 55% Sm^{2+}, one sees some broadening of the peak toward the position expected for the pure Sm^{2+} system. As the material is further cooled to 100 K, the peak shifts up nearer the position of the $Sm^{2+}S$ peak.

The phonon results show that the LA phonons are soft in the mixed valence phase, and as one approaches the Sm^{2+} single valence phase, the phonons shift to their normal positions. Detailed analysis of the phonon results is in progress at the present time but is quite difficult because of strong coupling between the electronic system and the lattice.

1. I B M Thomas Watson Research Center, Yorktown Heights, New York.

2. R. A. Pollak et al., *Phys. Rev. Lett.* 33, 820 (1974).
3. J. L. Freeouf et al., *Phys. Rev. Lett.* 33, 161 (1974).
4. J. M. Coey et al., *Phys. Rev. B* 14, 3744 (1976).
5. S. M. Shapiro, *Physical Review* (to be published).

MAGNETIC PROPERTIES

GENERAL RELATIONSHIP BETWEEN CONCENTRATION DERIVATIVES AND CORRELATION FUNCTIONS FOR ALLOYS[1]

R. A. Medina[2] J. W. Garland[3]

A general relationship is derived between the concentration derivative of any ensemble-averaged

quantity and the correlation function of that quantity with fluctuations in the concentration. This relationship is then used to obtain general formulas for the concentration derivatives of the magnetization $M(\mathbf{K})$ and of the Warren short-range-order parameters $\alpha(\mathbf{R})$ for the case of binary substitutional alloys. The use of these formulas in the analysis of diffuse elastic neutron scattering data and in the analysis of the effects of short-range order is discussed briefly.

1. Abstract of paper: *Phys. Rev.* 14, 5060 (1976).
2. IVIC graduate participant from Georgia Institute of Technology, Atlanta. Present address: Instituto Venezolano de Investigaciones Cientificas, Caracas, Venezuela.
3. Summer research participant from University of Illinois at Chicago Circle.

POLARIZED NEUTRON STUDY OF FERROMAGNETIC Ni-Cu ALLOYS: EVIDENCE FOR A MAGNETIC ENVIRONMENT EFFECT[1]

R. A. Medina[2] J. W. Cable

We measured the magnetic diffuse scattering of polarized neutrons from ferromagnetic Ni-Cu alloys with 19.8, 29.6, and 52.5 at. % copper at 4.2 K. The data show that the copper atoms are not polarized and that the negative polarization exists only around the nickel sites. Assuming that the nickel moments are a function of the moments of the neighboring atoms, we obtain an analytical expression for the polarized neutron cross section which describes the data well. The magnetic environment model is also shown to reproduce the moment disturbances of other dilute nickel-based alloys. A Stoner type of calculation shows that 20–40% interatomic exchange is needed to reproduce the Ni-Cu magnetization and cross sections; within the same calculation each copper atom induces a 1–2% moment reduction on its nickel neighbors for any given exchange field.

1. Abstract of paper: *Phys. Rev. B* 15, 1539 (1977).
2. IVIC graduate participant from Georgia Institute of Technology, Atlanta. Present address: Instituto Venezolano de Investigaciones Cientificas, Caracas, Venezuela.

NEUTRON STUDY OF LOCAL ENVIRONMENT EFFECTS IN FERROMAGNETIC Ni-Rh ALLOYS[1]

J. W. Cable

The ferromagnetic Ni-Rh alloys exhibit an anomalous magnetization vs. concentration behavior.[2,3] With increasing rhodium content, the spontaneous magnetization first increases by about 2 μ_B per rhodium, then passes through a maximum of near 4 at. % rhodium before decreasing to zero at the critical concentration of 37 at. % rhodium. A neutron measurement[4] in the dilute rhodium region shows that the initial increase in magnetization is due to a large rhodium moment (about 2 μ_B). One aim of the present neutron experiment is to determine the spatial distribution of the magnetic moments to determine whether the rapid loss of moment at higher concentrations is associated with competing ferro- and antiferromagnetic interactions, as in the Ni-Mn system, or with some other local environment effect that destroys this large rhodium moment. Another aim of the experiment is to answer a question raised by the magnetization results[3] in the critical region which indicate the presence of magnetic clusters similar to those found[5,6] for Ni-Cu alloys. This suggests that magnetic environment effects occur in Ni-Rh because such effects are required[7–9] to explain the neutron data[8–10] for the Ni-Cu alloys. In this paper we explore this possibility by extending a recently developed[9] magnetic environment model for nonmagnetic impurities in nickel to the case of magnetic impurities in nickel and by fitting this model to the neutron data.

Magnetic diffuse scattering cross sections were measured by both the unpolarized-neutron, field-off minus field-on method and the polarized-neutron, spin-up minus spin-down method. The unpolarized cross section is given by

$$\Delta\, d\sigma/d\Omega_{\text{unpol}}(\mathbf{K}) = 0.0484c(1-c)T(\mathbf{K})\,, \qquad (1)$$

in which c is the fractional impurity content and $T(\mathbf{K})$ is the Fourier transform of a two-site, moment-moment correlation. The polarized cross section is

$$\Delta\, d\sigma/d\Omega_{\text{pol}}(\mathbf{K}) = 1.08c(1-c)(b_i - b_h)M(\mathbf{K})\,, \quad (2)$$

where b_i and b_h are the impurity and host nuclear scattering amplitudes and $M(\mathbf{K})$ is the Fourier

transform of a site occupation-moment correlation. Measured $M(\mathbf{K})$ and $T(\mathbf{K})^{1/2}$ functions are shown in Fig. 4.24; the average nickel and rhodium moment behavior obtained by fitting $M(\mathbf{K})$ to the Marshall model[11] is given in Fig. 4.25.

The agreement between $M(0)$ and $d\bar{\mu}/dc$ in Fig. 4.24 shows that the magnetic moment fluctuations are due to local environment effects. The range of these effects increases with increasing rhodium content indicating that the magnetic environment is an important factor in the moment distribution of these alloys. The $M(\mathbf{K})$ data are fitted to an extended version of a previously described magnetic-environment model with physically reasonable parameters. The magnetic parameter Γ, which appears as an exchange enhancement factor that determines the K dependence, is found to approach the correct limits at both extremes of the ferromagnetic region. This parameter approaches unity at the critical composition, which is lower here (37 at. % rhodium) than for Ni-Cu alloys (56 at. % copper). This approach to unity depends on the details of the *d*-band structure for the *ferromagnetic* alloys. Such calculations are not yet available for comparison with the present results.

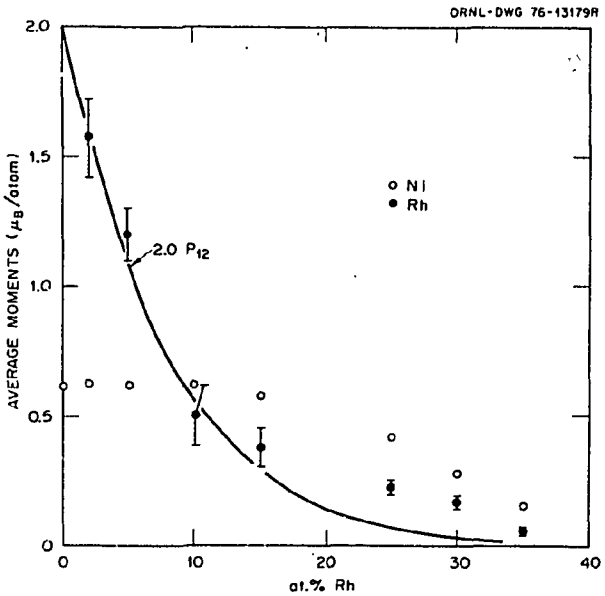

Fig. 4.25. The average moments at rhodium and nickel sites vs concentration for Ni-Rh alloys. The expression P_{12} is the probability that an atom has 12 nickel nearest neighbors.

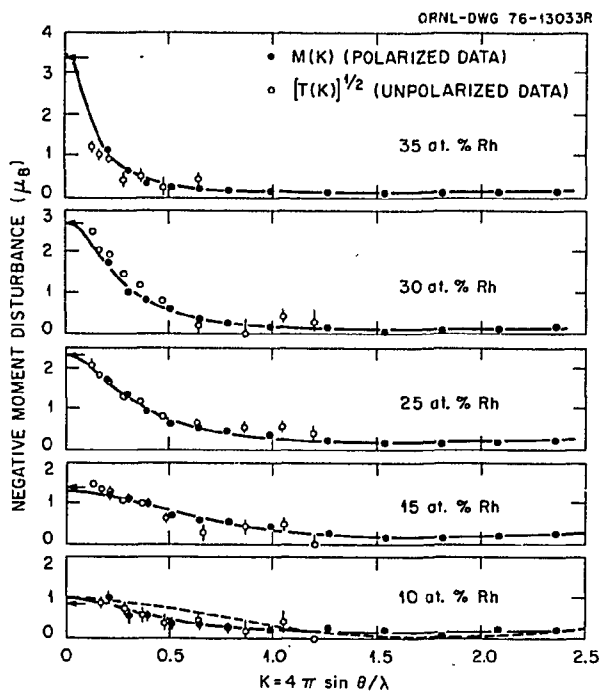

Fig. 4.24. The *K*-dependent magnetic moment disturbances for concentrated Ni-Rh alloys. The solid curves are fitted to the Marshall model while the dashed curve for 10 at. % rhodium is a calculation based on the magnetic environment model. The arrows at $K = 0$ represent the magnetization values of $d\bar{\mu}/dc$.

It seems unlikely that the rapid decrease in the average rhodium moment arises from antiferromagnetic Rh-Rh interactions since an antiparallel correlation of aligned rhodium moments should appear as a peak in the $M(\mathbf{K})$ or $[T(\mathbf{K})]^{1/2}$ function near $\mathbf{K} = 1.5$ Å^{-1} where a dip is actually observed. A more likely mechanism is a strong local environment effect that destroys, or at least drastically reduces, the ferromagnetic rhodium moment. Within this framework, it is interesting to compare the rhodium moment behavior with the probability of nearest-neighbor configurations. One finds that the rapid decrease is best described by a P_{12} dependence where $P_{12} = (1 - c)^{12}$ is the probability that an atom has 12 nickel nearest neighbors. This is illustrated by the curve labeled $2P_{12}$ (Fig. 4.25) that passes through the inner data points and suggests a moment of 2 μ_B for isolated rhodium atoms but a much smaller moment for those rhodium atoms with one or more rhodium nearest neighbors.

1. Summary of paper: *Phys. Rev. B* 15, 3477 (1977).
2. J. Crangle and D. Parsons, *Proc. R. Soc. London* A255, 509 (1960).
3. W. C. Muellner and J. S. Kouvel, *Phys. Rev. B* 11, 4552 (1975).

4. J. B. Comly, T. M. Holden, and G. G. Low, *J. Phys. C* 1, 458 (1968).
5. J. S. Kouvel and J. B. Comly, *Phys. Rev. Lett.* 24, 598 (1970).
6. T. J. Hicks et al., *Phys. Rev. Lett.* 22, 531 (1969).
7. J. W. Garland and A. Gonis, p. 79 in *Magnetism in Alloys*, ed. by P. A. Beck and J. T. Waber, AIME, New York, 1972.
8. A. T. Aldred et al., *Phys. Rev. B* 7, 218 (1973).
9. R. A. Medina and J. W. Cable, *Phys. Rev. B* 15, 1539 (1977).
10. J. W. Cable, E. O. Wollan, and H. R. Child, *Phys. Rev. Lett.* 22, 1256 (1969).
11. W. Marshall, *J. Phys. C* 1, 88 (1968).

A NEUTRON STUDY OF LOCAL ENVIRONMENT EFFECTS AND MAGNETIC CLUSTERING IN $Fe_{0.7}Al_{0.3}$[1]

J. W. Cable L. David[2] R. Parra[3]

Ordered Fe_3Al is one of the first alloys for which a local environment effect on the magnetic moment of an atom was demonstrated.[4] In this structure, the iron atoms on β sites have eight iron nearest neighbors and the same room-temperature moment as in bcc iron (2.18 μ_B), while those iron atoms on α sites have four iron and four aluminum nearest neighbors and moments of only 1.50 μ_B. The ordered structure is retained to 32 at. % aluminum with the excess aluminum tending to occupy the β sites.[5,6] The magnetization decreases rapidly with this excess aluminum, and beyond 30 at. % aluminum the system is no longer spontaneously ferromagnetic.[7,8] The magnetic behavior is anomalous in the 27 to 32 at. % aluminum region where the magnetization actually decreases with decreasing temperature.[7,8] Furthermore, mictomagnetism appears at low temperatures in this region, as indicated by shifted hysteresis loops on field cooling and by sharp cusps in the low field susceptibilities.[8] The 30 at. % alloy has a particularly unusual behavior in that the state of magnetic order changes from ferromagnetic to paramagnetic to mictomagnetic on cooling. Furthermore, the shape of the magnetization curves indicates the presence of superparamagnetic clusters in all of these ordered regions. This neutron study was undertaken to gain insight into this rather complicated behavior. Diffuse scattering measurements were made to characterize the moment distribution within the clusters; Bragg scattering measurements were made to further refine the magnetic moment dependence on local environment.

Neutron diffuse scattering measurements were made on a polycrystalline sample of $Fe_{0.7}Al_{0.3}$ furnished by P. A. Beck. The observed cross sections exhibit a sharp increase at small K indicating the presence of clustering. The strong temperature dependence of these cross sections shows that most of this clustering is of magnetic origin. Remarkably, this is a continuous function without any anomalous behavior at the transition temperatures given by the magnetization data[8] which show that this alloy is ferromagnetic below T_C = 400 K, paramagnetic below the inverse Curie temperature, T_i = 170 K, and mictomagnetic below the freezing temperature, T_f = 92 K. These cross section data show that ferromagnetic clusters are present through all of these regions and that the ordering transitions result from the coupling of these clusters.

In the Fe_3Al type of order, iron atoms preferentially occupy the α sites at (000, $\frac{1}{2}\frac{1}{2}\frac{1}{2}$) fcc and the β sites at ($\frac{3}{4}\frac{1}{4}\frac{1}{4}$) fcc, while the aluminum atoms tend to occupy the β sites at ($\frac{1}{4}\frac{1}{4}\frac{1}{4}$) fcc. There are three types of reflections with the nuclear structure factors:

$$\begin{aligned} F_{hk\ell} &= 16\langle b\rangle\,, && h+k+\ell = 4n\,,\\ &= 4(b_{Fe}-b_{Al})S\,, && h+k+\ell = 4n+2\,, \quad (1)\\ &= 4i(b_{Fe}-b_{Al})S_{\beta\lambda}\,, && h+k+\ell = 2n+1\,. \end{aligned}$$

Here, $\langle b\rangle = (1-c)b_{Fe} + cb_{Al}$, $S = 2r_\alpha - r_\beta - \omega_\gamma$, and $S_{\beta\gamma} = r_\beta - \omega_\gamma$, where the r's and ω's denote the fraction of the "rightly" or "wrongly" occupied lattice sites indicated by the subscripts. The fractional site occupations are determined from the identity $2r_\alpha + r_\beta + \omega_\gamma = 4(1-c)$ and the two long-range-order parameters S and $S_{\beta\gamma}$.

Nuclear intensities, measured at room temperature in zero field with 1.7 Å unpolarized neutrons, yield $S = 1.23 \pm 0.07$, $S_{\beta\gamma} = 0.607 \pm 0.025$, $r_\alpha = 1.01 \pm 0.02$ (maximum $r_\alpha = 1.00$), $r_\beta = 0.70 \pm 0.02$, and $\omega_\gamma = 0.09 \pm 0.02$. These fractional site occupations are consistent with those previously reported for the FeAl system.[4-6]

Magnetic structure factors were determined by the usual polarized-neutron, flipping-ratio method. Such measurements yield magnetic to nuclear structure factor ratios which, for the three types of reflections, are given by

$$(F_M/F_N)_{4n} = \langle p\rangle/\langle b\rangle\,, \quad (2)$$

$$(F_M/F_N)_{4n+2} = (2r_\alpha p_\alpha - r_\beta p_\beta - \omega_\gamma p_\gamma)(b_{Fe}-b_{Al})S\,, \quad (3)$$

$$(F_M/F_N)_{2n+1} = (r_\beta p_\beta - \omega_\gamma p_\gamma)/(b_{Fe}-b_{Al})S_{\beta\gamma}\,. \quad (4)$$

Here, $4\langle p\rangle = 2r_\alpha p_\alpha + r_\beta p_\beta + \omega_\gamma p_\gamma$, and the p's are the magnetic scattering amplitudes of iron atoms on the subscripted lattice sites. These are related to the iron

moments by $p_i = 0.27\ \mu_i f$, where f is the form factor that is independent[4,9] of the lattice site. Because the site occupations, long-range-order parameters, and form factors [9] have all been determined, the μ_i's are directly obtained by appropriate combinations of these F_M/F_N ratios for the three types of reflections. Average moment values on α and β sites and at temperatures corresponding to the three states of order are given in Table 4.2.

The rapid decrease in magnetization of the ordered Fe-Al alloys between 25 and 32 at. % aluminum is clearly associated with the introduction of aluminum atoms onto β sites. This fact, along with the neutron observation[4] of a reduced α-site moment in Fe_3Al and the Mössbauer observation[10] of three hyperfine fields in the 22 to 26 at. % aluminum region, led to a model in which the iron moment was assumed[10-12] to vary with the number of nearest-neighbor iron atoms, n. In this model, it is generally assumed that the iron moment remains at 2.2 μ_B for $n = 8$, 7, and 6 since the average moment of the disordered alloys out to 23 at. % aluminum decreases, as is done in simple dilution. Also, because the 32 to 50 at. % aluminum alloys are paramagnetic, iron atoms with $n = 0$ and 1 are assumed to have no moment. This leaves only the n = 2, 3, 4, and 5 cases to be assigned. The site occupation and site moment determinations for this 30 at. % alloy permit a refinement of the previous assignments.[7-9] If P_n^{α} is defined as the probability that an α site has n iron nearest neighbors, then

$$\langle \mu_\alpha \rangle = \sum_n P_n^{\alpha}\ \mu_\alpha(n) .$$

The observed $^{\alpha}P_n$ values for the two alloys considered for the moment assignment are shown in the lower part of Fig. 4.26. The $\mu_\alpha(n)$ values obtained by assuming $2.2\ \mu_B = \mu_\alpha(8) = \mu_\alpha(7) = \mu_\alpha(6) \geq \mu_\alpha(5) \geq \mu_\alpha(4) \geq \mu_\alpha(3) \geq \mu_\alpha(2) \geq 0$ are given in the upper part of the figure. These exhibit a strong local environment effect for just those configurations that occur with the highest probabilities in the 25 to 32 at. % aluminum region.

Table 4.2. Spontaneous and saturation moments for $Fe_{0.7}Al_{0.3}$

Temperature, K	$\langle\mu_\alpha\rangle_0$	$\langle\mu_\alpha\rangle_\infty$	$\langle\mu_\beta\rangle_0$	$\langle\mu_\beta\rangle_\infty$
220	0.324	0.656	0.780	1.57
110	0	0.646	0	1.62
5	0	0.613	0	1.56

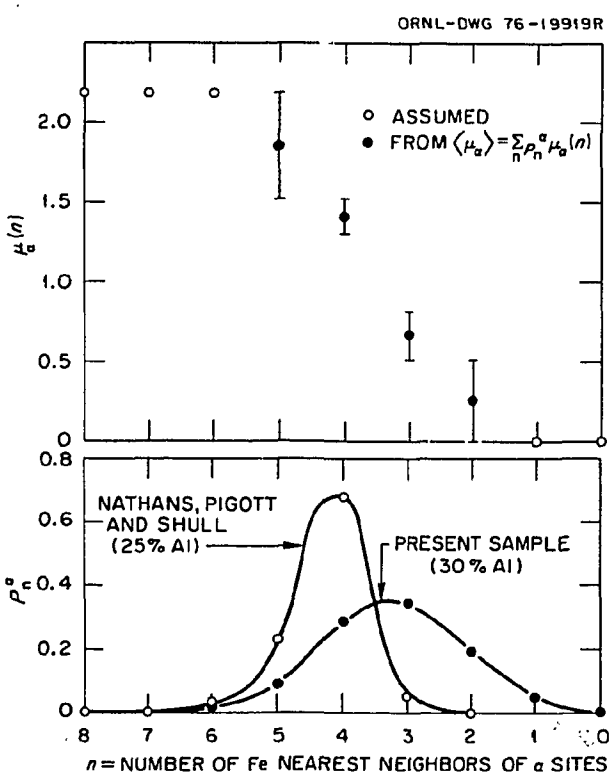

Fig. 4.26. Values of $^{\alpha}P_n$ and $\mu_\alpha(n)$ for ordered Fe-Al alloys. The lower figure shows the probability distributions used to obtain the upper figure.

1. Summary of paper: *Physical Review* (in press).
2. Guest scientist from Instituto Venezolano de Investigaciones Cientificas, Caracas, Venezuela.
3. IVIC graduate participant from Georgia Institute of Technology, Atlanta.
4. R. Nathans, M. T. Pigott, and C. G. Shull, *J. Phys. Chem. Solids* 6, 38 (1958).
5. A. J. Bradley and A. H. Jay, *Proc. R. Soc. London, Ser. A* 136, 210 (1932).
6. H. Okamoto and P. A. Beck, *Metall. Trans.* 2, 569 (1971).
7. A. Arrott and H. Sato, *Phys. Rev.* 114, 1420 (1959).
8. R. D. Shull, H. Okamoto, and P. A. Beck, *Solid State Commun.* 20, 863 (1976).
9. S. J. Pickart and R. Nathans, *Phys. Rev.* 123, 1163 (1961).
10. E. A. Friedman and W. J. Nicholson, *J. Appl. Phys.* 34, 1048 (1963).
11. P. A. Beck, *Metall. Trans.* 2, 2015 (1971).
12. H. Okamoto and P. A. Beck, *Monatsh. Chem.* 103, 907 (1972).

POLARIZED NEUTRON STUDY OF THE MAGNETIC MOMENT DISTRIBUTION IN PdMn Alloys[1]

J. W. Cable L. David[2]

Recent magnetization measurements[3,4] on dilute PdMn alloys show giant moment behavior similar to

that observed earlier for the PdFe[5] and PdCo[6] systems. At low concentrations of iron or cobalt impurities in palladium, the magnetic moment per impurity is about 10 μ_B, but neutron diffuse scattering[7-10] shows only about 3 μ_B per iron and 2 μ_B per cobalt localized at the impurity sites with the remainder being induced in the surrounding palladium atoms. For manganese impurities the giant moment is about 7.5 μ_B per impurity,[3,4] but some uncertainty still exists regarding what part of that is localized at manganese sites. Specific heat data[11] yield a spin value of 2.4 ± 0.2, which suggests 5 μ_B at the manganese sites; this is supported by neutron diffuse scattering results,[12] which give 5.5 ± 0.5 μ_B at the manganese site. However, this implies an electronic configuration with only five *d* electrons for manganese dissolved in a transition metal, whereas at least six *d* electrons and a maximum moment of $4\mu_B$ per manganese are expected. Also, this 5.5-μ_B value is larger than was obtained by paramagnetic scattering from a 10 at. % manganese alloy (3.3 ± 0.4 μ_B)[13] and by Bragg scattering from an ordered 25 at. % manganese alloy (4.0 ± 0.2 μ_B).[14] The diffuse scattering measurement[12] was made with unpolarized neutrons at a sample temperature near the Curie temperature and, since this method measures all moment-moment spatial correlations, high moment values could be obtained in the critical region. We decided that a determination of the manganese moment in palladium by the polarized-neutron diffuse scattering method was desirable. Here, only magnetic moment-site occupation correlations appear, and the measurements are not complicated by possible critical scattering effects.

In the polarized-neutron diffuse scattering experiment the sample is magnetized perpendicular to the scattering plane. In this geometry, the difference between the cross sections for incident neutrons polarized parallel and antiparallel to the magnetization is

$$\Delta\, d\sigma/d\Omega\,(\mathbf{K}) = 1.08c(1-c)(b_i - b_h)M(\mathbf{K}) ,$$

where c is the impurity concentration, b_i and b_h are the impurity and host nuclear scattering amplitudes, and $c(1-c)M(\mathbf{K})$ is the Fourier transform of the moment-site occupation correlation,

$$\langle (p_{n+R} - c)\mu_n(\mathbf{K}) \rangle .$$

Here, p_{n+R} is the number of impurity atoms (0 or 1) at $\mathbf{n}+\mathbf{R}$ and $\mu_n(\mathbf{K})$ is the moment-form factor product at site n. For polycrystalline samples, the spherical average of $M(\mathbf{K})$ at large K approaches $\langle \mu_i(K) \rangle - \langle \mu_h(K) \rangle$, while in the $K = 0$ limit, $M(0) = S(0)\, d\bar{\mu}/dc$ provided that the moment fluctuations are due to local environment effects. Thus, $S(\mathbf{K})$ is the usual short-range-order scattering function defined as the Fourier transform of

$$\langle (p_{n+R} - c)(p_n - c) \rangle / c(1-c) ,$$

and $d\bar{\mu}/dc$ is the concentration derivative of the average moment as determined from a bulk magnetization measurement. The observed $M(K)$ functions are shown in Fig. 4.27; the corresponding $\langle \mu_{Pd} \rangle$ and $\langle M_{Mn} \rangle$ values are given in Table 4.3.

Table. 4.3. Individual magnetic moments of PdMn alloys at 4.2 K and 45 kOe

Manganese, at. %	$\bar{\mu}$	$\langle \mu_{Pd} \rangle$	$\langle \mu_{Mn} \rangle$	$\mu_{Mn}{}^0$
0.23	0.016[a]	0.008	3.6	3.7[b]
0.46	0.030	0.012	4.0	4.3
0.99	0.058	0.024	3.5	4.0
1.91	0.099	0.034	3.5	4.4
	±1%	±10%	±0.3	±0.3

[a]The values in this column are bulk magnetizations from ref. 4 expressed in μ_B per atom.

[b]The values in this column are from $\langle \mu_{Mn} \rangle = (1-c)^{12}\, \mu_{Mn}{}^0$.

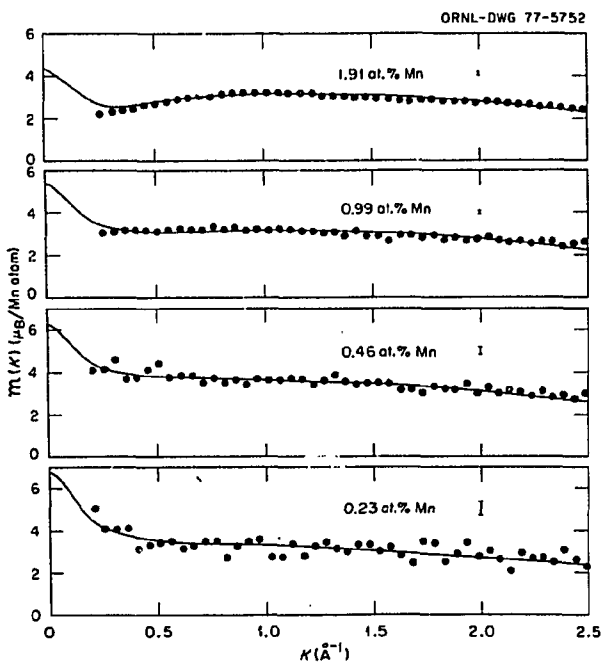

Fig. 4.27. $M(K)$ functions for some PdMn alloys at 4.2 K and 45 kOe. The solid curves are calculated for the magnetic environment model using the moment values in Table 4.3 and $\Gamma = 0.975$. A small amount of positional short-range order is included.

The polarized-neutron $M(K)$ functions and the bulk magnetization data for PdMn alloys can be brought into agreement by assuming a long-ranged impurity-induced moment disturbance in the palladium similar to that found[9,10] for PdFe and PdCo alloys. A one-parameter magnetic environment model reproduces this moment disturbance in PdFe and PdCo with parameters in the expected range. The same parameters carried over to the PdMn case are consistent with the observations, which are, however, severely limited in the small K region where most of this effect occurs. At the 1 to 2 at. % manganese level the $M(K)$ functions show evidence of an anticorrelation, which we interpret as the combined effects of positional short-range order and manganese spin reversal. The configurational aspects of the manganese spin reversal and the response of antiparallel manganese atom pairs to an applied field are crucial to understanding the magnetization behavior of these alloys. In the model that we have used, only the fraction $(1-c)^{12}$ of the manganese atoms have all palladium nearest neighbors and, with their surrounding palladium polarization clouds, are free to respond to an applied field. The remaining manganese moments in these dilute alloys are coupled together in antiferromagnetic pairs; these must be broken down by the applied field before magnetization can occur. Star, Foner, and McNiff[4] find normal Brillouin behavior at very low manganese content where essentially no manganese atom pairs occur, but note departures from this at higher manganese levels where the field required for saturation increases with increasing manganese content. They estimate that an antiferromagnetic coupling as large as 50 K is required to describe their high-field magnetizations within the molecular-field model. In that case, the 45 kOe applied in this experiment produces essentially no magnetization of the manganese atom pairs

$$[\mu H/kT \cong 0.24 \text{ for } \mu_{Mn}{}^{0} = 4\ \mu_B]$$

but about 96% saturation of the isolated manganese moments and their associated polarization clouds. The $\langle\mu_{Pd}\rangle$ and $\langle\mu_{Mn}\rangle$ values in Table 4.3 should therefore be increased by about 4% to obtain the saturation values. The $\mu_{Mn}{}^{0}$ values are obtained from $\langle\mu_{Mn}\rangle = (1-c)^{12}\mu_{Mn}{}^{0}$ and thus correspond to the random alloy with a nearest-neighbor spin-reversal mechanism. Actually, the short-range order in these alloys tends to isolate the manganese atoms, and this would decrease $\mu_{Mn}{}^{0}$. On the other hand, a longer ranged spin-reversal mechanism would tend to increase $\mu_{Mn}{}^{0}$. Because of these uncertainties, the best $\mu_{Mn}{}^{0}$ determination comes from the two more dilute alloys for which we obtain 3.8 ± 0.3 and $4.4 \pm 0.3\ \mu_B$ at saturation. These are significantly smaller than was deduced from the specific heat[11] and unpolarized neutron[12] data but are consistent with the expected electronic configuration of a manganese atom dissolved in palladium.

1. Summary of paper: *Physical Review* (in press).
2. Guest scientist from Instituto Venezolano de Investigaciones Cientificas, Caracas, Venezuela.
3. W. M. Star, S. Foner, and E. J. McNiff, *Phys. Lett. A* **39**, 189 (1972).
4. W. M. Star, S. Foner, and E. J. McNiff, *Phys. Rev. B* **12**, 2690 (1975).
5. J. Crangle, *Philos. Mag.* **5**, 335 (1960).
6. R. M. Bozorth et al., *Phys. Rev.* **122**, 1157 (1961).
7. J. W. Cable, E. O. Wollan, and W. C. Koehler, *J. Appl. Phys.* **34**, 1189 (1963).
8. J. W. Cable, E. O. Wollan, and W. C. Koehler, *Phys. Rev. A* **138**, 755 (1965).
9. G. G. Low and T. M. Holden, *Proc. Phys. Soc., London* **89**, 119 (1966).
10. T. J. Hicks, T. M. Holden, and G. G. Low, *J. Phys. C* **1**, 528 (1968).
11. B. M. Boerstoel, J. J. Zwart, and J. Hansen, *Physica* **57**, 379 (1972).
12. C. J. de Pater, C. van Dijk, and G. J. Nieuwenhuys, *J. Phys. F* **5**, L58 (1975).
13. N. Ahmed and T. J. Hicks, *J. Phys. F* **4**, L124 (1974).
14. J. W. Cable et al., *Phys. Rev.* **128**, 2118 (1962).

FIELD-INDUCED MAGNETIC DENSITY IN THE PARAMAGNETIC COMPOUND $LuCo_2$[1]

D. Gignoux[2] W. C. Koehler
F. Givord[2] R. M. Moon

The magnetization density induced in $LuCo_2$ by an applied magnetic field was measured by means of polarized neutron diffraction. The measurements were performed on a single crystal at 100 K in an applied field of 57.2 kOe. The observed density is localized on cobalt atoms with a form factor that is, within the experimental accuracy, similar to that of $3d$ electrons in cobalt metal. Weak additional magnetic amplitudes reveal a nonuniform polarization of the conduction band. Its mean value is opposite to the cobalt moment, as is found in cobalt metal.

1. Abstract of paper: *J. Magn. Magn. Mater.* **5**, 172, (1977).
2. Laboratoire Louis Néel, C.N.R.S., Grenoble, France.

DETERMINATION OF COBALT BEHAVIOR IN $TmCo_2$ AND $HoCo_2$ BY MEANS OF POLARIZED NEUTRON DIFFRACTION[1]

D. Gignoux[2] F. Givord[2] W. C. Koehler

The determination, from polarized neutron diffraction measurements, of the cobalt moment in $HoCo_2$ and $TmCo_2$ at various temperatures shows that the cobalt paramagnetic susceptibility is of Pauli type. Below the ordering temperature, a large increase of the cobalt susceptibility, related to the large value of the molecular field, was observed.

1. Abstract of paper: *Physica* **86-88 B + C**, 165 (1977).
2. Laboratoire Louis Néel, C.N.R.S., Grenoble, France.

FIELD-INDUCED PARAMAGNETIC FORM FACTOR IN METALLIC SCANDIUM[1]

W. C. Koehler R. M. Moon

The magnetic form factor of metallic scandium has been measured at a temperature of 100 K in an applied field of 57.2 kOe by the polarized-neutron technique. Contrary to results on other 3*d* metals, the form factor is significantly different from that for the 3*d* electron in the free atom. Our results agree rather well with those of a calculation by Gupta and Freeman based on augmented plane wave (APW) functions.

1. Abstract of paper: *Phys. Rev. Lett.* **36**, 616 (1976).

POLARIZED NEUTRON DIFFRACTION BY SCANDIUM-NUCLEAR POLARIZATION

W. C. Koehler R. M. Moon

We have recently measured the induced-moment form factor in metallic scandium at 100 K in a field H of 57.2 kOe.[1] The measured polarization ratios are very close to unity so that some care is necessary to account for small perturbing effects. Among these, we thought, was a possible contribution, even at 100 K, from a partial polarization of the scandium nuclei.

To assess the importance of such a possible contribution, we first calculated the expected effect, using (1) published data on the spin ($I = {}^7/_2$), magnetic moment ($\mu = +4.7564$ nuclear magnetons), and coherent scattering amplitude ($b = 1.18 \times 10^{-12}$ cm) of scandium,[2] and (2) the quantity $(b^+ - b^-) = 1.20 \times 10^{-12}$ cm. in which $b^\pm$ are the scattering amplitudes for the states $I \pm {}^1/_2$ of the compound nucleus.[3]

In the notation of Moon, Riste, and Koehler,[4] the total amplitude for scattering from the ($\pm$) initial state to the ($\pm$) final state of the neutron is

$$U^{\pm\pm} = b \pm B\langle I_z \rangle , \tag{1}$$

where $B = (2I + 1)^{-1}(b^+ - b^-)$ and b is the coherent nuclear scattering amplitude. (In this discussion we neglect magnetic scattering for the time being.) The quantity $\langle I_z \rangle$ is the thermally averaged spin component given by

$$\langle I_z \rangle \frac{I(I+1)gH}{3kT} = \frac{I+1}{3}\frac{\mu H}{kT} , \tag{2}$$

when $\mu H/kT \ll 1$. The effective scattering amplitude is then

$$b_{\text{eff}} = b \pm \frac{I+1}{3(2I+1)}\frac{\mu H}{kT}(b^+ - b^-) = b \pm \frac{3}{16}\frac{\mu H}{kT}(b^+ - b^-) . \tag{3}$$

The residual polarization ratio may be expressed as

$$R - 1 = \frac{3\mu H}{4kT}\left(\frac{b^+ - b^-}{b}\right). \tag{4}$$

With the values given above for the several parameters and in a field of 57.2 kOe,

$$R - 1 = \frac{758}{T} \times 10^{-5} . \tag{5}$$

Thus at 100 K the magnitude of the contribution of nuclear polarization to the experimental polarization ratios is 7.6×10^{-5}, a quantity about equal to the contribution of the neutron spin-neutron orbit interaction and to the magnetic contributions for the higher index reflections.

We then undertook to measure the residual flipping ratio for a reflection, the (004), which has a very small magnetic contribution at 100 K, at several reduced temperatures. If nothing else changes, the slope of the curve $R - 1$ vs $1/T$ should be equal to 758×10^{-5}.

The experimental observations are shown in Fig. 4.28. A least squares fit of the data shown to the linear function $\alpha + \beta/T$ gives a value for $\beta = -(748 \pm 20) \times 10^{-5}$. This in turn can be interpreted as corresponding to a value for $b^+ - b^- = -(1.18 \pm 0.05) \times 10^{-12}$, a result

very close in magnitude to that of ref. 3 but of opposite sign.

The negative sign had been suspected by Chrien,[5] recently demonstrated by Marshak,[6] and confirmed in a remeasurement by Mériel.[7] In Mériel's new measurement he finds (tentatively) a value for $b^+ - b^- = -1.38 \times 10^{-12}$ cm. This is in much better accord with the published values of the total and coherent scattering cross sections, which yield a value for $|b^+ - b^-|$ of 1.45×10^{-12} cm, than the earlier value and our result of $b^+ - b^- = -1.18 \times 10^{-12}$ cm. We show the expected variation of $R - 1$ vs $1/T$ for $b^+ - b^- = -1.38 \times 10^{-12}$ cm as the dashed curve in Fig. 4.28. Several reasons suggest themselves for the difference: nonconstancy, as assumed, of the paramagnetic susceptibility of scandium; the presence of paramagnetic impurities such as other rare earths; the presence of interstitial hydrogen; and systematic errors in our temperature measurement.

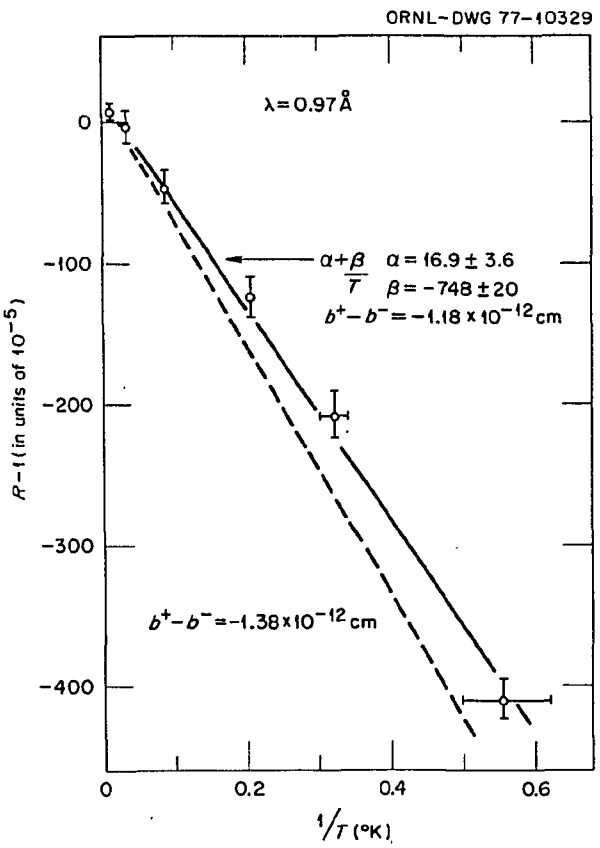

Fig. 4.28. Residual flipping ratio $R - 1$ of (004) reflection in scandium vs $1/T$. The solid line is a least squares fit of the data which yields $b^+ - b^- = -1.18 \times 10^{-12}$ cm. The dashed curve is calculated for $b^+ - b^- = -1.38 \times 10^{-12}$ cm.

Obtained from the same material prepared at Ames and studied by Spedding and Croat,[8] the scandium single crystal that we studied was of very high purity. The susceptibility of this material changes only about 2% in the temperature range 2 to 10 K and less than 10% in the range 2 to 100 K. Since the magnetic contribution to the (004) is very small, the effect of changes in susceptibility or the presence of paramagnetic impurities is negligible. Spectrochemical analysis showed only a few parts per million atomic of other rare earths.

The presence of hydrogen in the sample can have serious consequences in our measurements and in Mériel's. A typical hydrogen impurity concentration could be 250 ppm by weight.[8] Such an amount of hydrogen will give a contribution to the residual flipping ratio of

$$(R - 1)_H = -\frac{99}{T} \times 10^{-5} \qquad (6)$$

Because this has a negative sign, it will tend to make the apparent slope of the $R - 1$ vs $1/T$ curve more negative. If substantial amounts of hydrogen were indeed present in our sample, the data for scandium corrected for the hydrogen polarization would lead to a value of $|b^+ - b^-|$ even smaller than 1.18×10^{-12} cm.

The manner in which the temperature is measured in our experiment can produce uncertainties of the order of 0.2 K. At the lowest temperature such an uncertainty is enough to bring our data into agreement with the slope calculated from Mériel's recent results. Nevertheless, the aim of the experiment, to demonstrate and evaluate a small correction to the polarization ratios at 100 K due to nuclear polarization, has been achieved. The sign of $b^+ - b^-$ is now well established; within reasonable limits, the magnitude is also established.

1. W. C. Koehler and R. M. Moon, *Phys. Rev. Lett.* **36**, 616 (1976).
2. W. O. Milligan et al., *J. Chem. Phys.* **58**, 5514 (1973).
3. P. Roubeau et al., *Phys. Rev. Lett.* **33**, 102 (1974).
4. R. M. Moon, T. Riste, and W. C. Koehler, *Phys. Rev.* **181**, 920 (1969).
5. R. Chrien, private communication.
6. H. Marshak, private communication.
7. P. Mériel, private communication.
8. F. H. Spedding and J. J. Croat, *J. Chem. Phys.* **58**, 5514 (1973).

MAGNETIC FORM FACTOR OF 3*d* AND 4*d* PARAMAGNETIC METALS[1]

R. M. Moon W. C. Koehler J. W. Cable

A survey of published results on magnetic form factors of Cr, V, Sc, and Pd is presented, together with a preliminary report on new results for Ti, Y, and Nb. The data clearly show the inadequacy of free atom or extreme tight-binding models in describing the outer electronic density in transition metals. In several cases there is good agreement with APW calculations, giving confidence in the accuracy of the APW functions. Experimental errors limiting the accuracy of polarized-beam measurements are discussed.

1. Abstract of paper: p. 577 in *Proceedings of the Conference on Neutron Scattering*, vol. II, ed. by R. M. Moon, ERDA CONF-760601-P2, Oak Ridge, Tenn., 1976.

MAGNETIC FORM FACTOR OF Eu^{2+} in EuO[1]

J. W. Cable W. C. Koehler

It has long been expected that solid state effects would be unimportant for the 4*f* electrons in the heavy rare earths and that the 4*f* charge and spin densities should be well approximated by free ion wave functions. This seems to be the case for the heavy rare earth metals gadolinium and erbium for which good agreement is obtained between the observed [2,3] neutron magnetic form factors and those calculated[3,4] for the tripositive ions using relativistic Dirac-Fock wave functions. The situation is less clear for rare earth oxides. Neutron polarization analysis data for Gd_2O_3 were originally interpreted[2] to indicate a significant contraction (about 10%) of the 4*f* spin density relative to that in the metal. Although most of this difference has now been removed by a careful reanalysis[5] including spin correlations, it was this result that provided the original motivation for this neutron study of the magnetic form factor of EuO.

In many respects EuO is the ideal rare-earth-containing insulator for such a neutron study. It is ferromagnetic[6] in a readily accessible temperature region (T_c = 69.3 K) and has the simple rock-salt structure. The europium is divalent with an $^8S_{7/2}$ ground state so the magnetic moment is all spin moment and, since the 4*f* shell is half filled, the spin and charge densities are the same. The big disadvantage for neutrons is the high absorption cross section of the europium (about 1600 b at 1 Å), which means that small crystals and relatively long counting times are required.

Nevertheless, flipping ratio measurements were successfully made on two single crystals of EuO in a vertical magnetizing field of 20 kOe. One of these crystals was pillar shaped with dimensions 0.6 × 1.0 × 2.5 mm; the other was disk shaped with thickness 0.46 mm and a diameter of approximately 5 mm. In each case the crystal was mounted with a (110) direction parallel to the applied field; data were collected for the first 21 Bragg reflections at $\lambda = 0.75$ Å and for the first 14 reflections at 1.067 Å. A plutonium filter was used to avoid $\lambda/2$ beam contamination at 1.067 Å, and calculations showed no significant $\lambda/2$ correction at either wavelength. Corrections for incomplete incident polarization, flipper efficiency, and sample depolarization were applied. Observations on equivalent reflections with different path lengths through the crystals gave no indication of extinction as should be expected for these highly absorbing crystals.

Prepared at the IBM Thomas J. Watson Research Center, the EuO single crystals used in this study were supplied to us by J. B. Torrance. They are nominally 1% deficient in europium and therefore remain insulating at low temperature.[7] The actual europium content was established from magnetization measurements made on one of the crystals by J. S. Kouvel. If x is defined as the fraction of vacant europium sites, then $2x Eu^{3+}$ ions and $(1 - 3x)Eu^{2+}$ ions are on the europium sites. The observed magnetization of 6.73 μ_B per europium site at 4.2 K and 20 kOe corresponds to $x = 0.013$ assuming 7 μ_B per Eu^{2+} and zero moment for the Eu^{3+} and O^{2-} ions.

Some 284 separate measurements were made with approximately four runs per reflection for each crystal at each wavelength. The corrected flipping ratios for the two crystals were in good agreement, so averaged data were used to obtain the experimental $\bar{\mu}f$ values shown in Fig. 4.29 where they are plotted vs $(\sin\theta)/\lambda$. These values exhibit the smooth variation expected for the spherically symmetric spin density of an *S*-state ion. However, the radial dependence differs from that calculated[8] from relativistic Dirac-Fock wave functions for the Eu^{2+} ion. This is shown in Fig. 4.29 where the solid curve is the calculated Dirac-Fock form factor normalized to the average moment of 6.73 μ_B. The observed form factor falls off more rapidly with $(\sin\theta)/\lambda$ and indicates an approximate 9% expansion of the 4*f* wave functions in EuO relative to those in the Eu^{2+} ion. This is

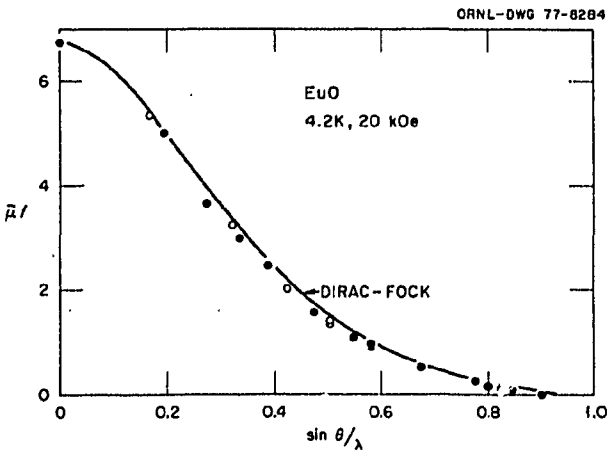

Fig. 4.29. Averaged $\bar{\mu}f$ data of EuO at 4.2 K and 20 kOe. The open (closed) data points are for all odd (even) *hkl* reflections with the point at the origin taken from the bulk magnetization. The solid curve was calculated for the Eu^{2+} ion from relativistic Dirac-Fock wave functions (ref. 8).

somewhat surprising because the free ion calculations give agreement with the observed form factors for Gd^{2+}[4] and Er^{3} and also for the Tb^{3+} ion in $Tb(OH)_3$.[9] However, recent molecular cluster calculations[10] show that small solid state effects may be expected in EuO. The calculations indicate a 4% expansion of the 4*f* wave functions in $(EuO_6)^{12-}$ clusters relative to those in the Eu^{2+} ion. The present results suggest an even larger effect in EuO.

1. Summary of paper: *Journal of Magnetism and Magnetic Materials* (in press).
2. R. M. Moon et al., *Phys. Rev. B* 5, 997 (1972).
3. C. Stassis et al., *Phys. Rev. B* 13, 3916 (1976).
4. A. J. Freeman and J. P. Desclaux, *Int. J. Magn.* 3, 311 (1972).
5. R. M. Moon and W. C. Koehler, *Phys. Rev. B* 11, 1609 (1975).
6. B. T. Matthias, R. M. Bozorth, and J. H. VanVleck, *Phys. Rev. Lett.* 7, 160 (1961).
7. M. W. Shafer, J. B. Torrance, and T. Penny, *J. Phys. Chem. Solids* 33, 2251 (1972).
8. A. J. Freeman and J. P. Desclaux, private communication.
9. G. H. Lander et al., *Phys. Rev. B* 8, 3237 (1973).
10. E. Byrom, D. E. Ellis, and A. J. Freeman, *Phys. Rev. B* 14, 3558 (1976).

MAGNETIC ORDERING IN THE LOWER VALENCE VANADIUM FLUORIDES[1]

R. F. Williamson[2] W.O.J. Boo[2]
W. C. Koehler

The tetragonal rutile compounds VF_2, MnF_2, CoF_2, and NiF_2 order antiferromagnetically at low temperatures. Ordered structures are of the *A-B* type except for VF_2. Strong interactions between nearest neighboring V(II) ions cause ordering in VF_2 to commence above 100 K as linear chains. Three-dimensional long-range ordering is hindered by the constraint that all nearest-neighboring V(II) ions have common second-nearest neighbors. Below 7 K the ordered structure consists of spirals along the *c* axis. LiV_2F_6 is also of the rutile type, but magnetic constraints existing in VF_2 are not present in this compound. Consequently, its magnetically ordered structure is different and occurs above 7 K. Ordering in the perovskite KVF_3 occurs at 130 K and is antiferromagnetic of the *G* type. Other perovskite-like compounds include orthorhombic $NaVF_3$ and mixed-valence compounds having tetragonal and hexagonal tungsten bronze structures. Ordering in these materials is complex because of constraints between neighboring vanadium ions.

1. Abstract of paper: *Proceedings of the Symposium on Recent Advances in Solid State Chemistry*, American Chemical Society, New Orleans, Louisiana, March 21-25, 1977 (in press).
2. University of Mississippi, University.

A NEUTRON STUDY OF THE ANTIFERROMAGNETIC ORDER IN Cr-Si ALLOYS[1]

J. W. Cable

Chromium has a sinusoidally modulated, antiferromagnetic structure[2] usually described as a static spin density wave in the conduction electrons[3] which is presumably stabilized by certain "nesting" features of the conduction band Fermi surface.[4] This model has been successfully used[5,6] to explain the magnetic structure changes caused by alloying with various transition metals. Such effects have been thoroughly investigated and fall basically into two categories: (1) those metals with the same or fewer outer electrons cause a decrease in T_N, magnetic moment, and the magnitude of the modulation wave vector **q** and (2) those metals with more outer electrons cause an increase in moment and **q** and produce the commensurate antiferromagnetic (CAF) structure above the 1% impurity level.

Much less is known about the effects of nontransition elements on the magnetic order of chromium, but there has been much recent activity[7-12] regarding the Cr-Si system. Electrical resistivity studies[7,10] show unusual step-type anomalies above the 1 at. % silicon

level, while magnetic susceptibility measurements[9,11] show that these are associated with magnetic ordering. By analogy with similar behavior in other systems of known magnetic order, it was suggested[9] that these anomalies indicate the development of the CAF structure. Support for this type of ordering is also gained from thermoelectric power[8] and dT_N/dP data.[12] The present study was undertaken to establish the type of magnetic order in these alloys by use of neutron diffraction methods.

Neutron diffraction measurements were made on polycrystalline samples of Cr-Si alloys containing 0.90, 1.37, 1.85, and 2.74 at. % silicon. Furnished to us by S. Arajs, these samples are from the same stock that was used in the susceptibility[9,11] and transport[6,7,11] studies.

The temperature dependence of the magnetic ordering in these alloys is summarized in Fig. 4.30. This necessarily schematic phase diagram indicates the stable regions of the three types of magnetic order. Below 1 at. % silicon the behavior is similar to that of pure chromium with a transition from the paramagnetic state to the transverse spin density wave (TSDW) state at T_N followed by a spin flip transition to a longitudinal spin density wave (LSDW) at lower temperature. Above 1.8 at. % silicon only the CAF structure ($q = 2\pi/a$) develops, while paramagnetic → CAF → TSDW transitions occur in the intermediate region. The shaded area between the TSDW and two-phase region is intended to represent thermal hysteresis effects. The magnitude of q is shown as the upper part of this figure. An increase in q occurs at low impurity levels followed by a collapse to $q = 1$ at the higher levels.

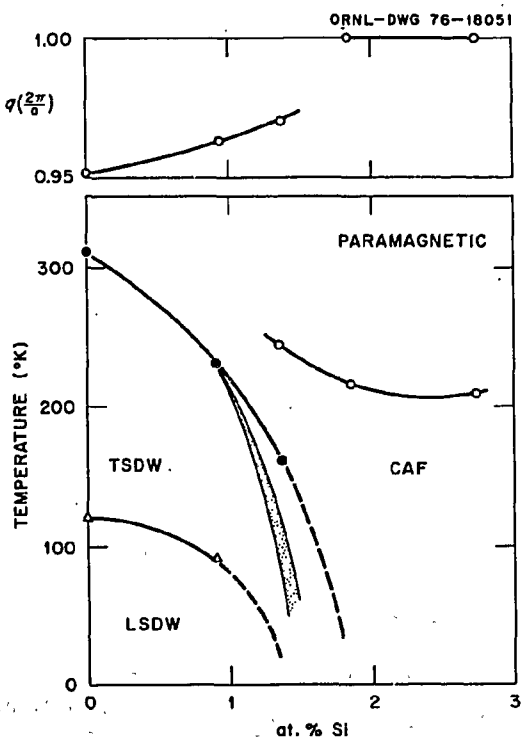

Fig. 4.30. Schematic phase diagram and q dependence for Cr-Si alloys.

The observed changes in magnetic order caused by the introduction of silicon into chromium are quite similar to the effects caused by transition metal impurities, such as manganese or iron, with more outer electrons than chromium. Within the rigid-band extension of the Lomer model,[4] this implies that silicon behaves as an electron donor in chromium. It has been suggested[12] that this is anomalous behavior because silicon has fewer outer electrons than chromium. This overlooks a basic difference in the electronic structure of transition metal and nontransition element inpurities in transition metal hosts. With transition metal impurities, the number of *sp* electrons is nearly the same inside the atomic volumes surrounding impurity and host sites, and any screening of excess charge is associated with the number of *d* electrons at these sites. In this case, e/a arguments can be used to decide whether charge transfer is to or from impurity sites. However, with nontransition element impurities, more *sp* electrons exist at the impurity sites, and this excess conduction electron charge is screened by the surrounding host atoms. Thus all of these elements behave as electron donors in transition metal hosts. This is perhaps best illustrated by the magnetization behavior of nickel-based alloys for which the average moment decreases at a rate proportional to the number of valence electrons of the nontransition element impurity. The present neutron results therefore show that silicon behaves as an electron donor in chromium, as was expected.

---

1. Summary of paper: *Journal of Magnetism and Magnetic Materials* (in press).
2. G. Shirane and W. J. Takei, *J. Phys. Soc. Jpn., Suppl. B-III* 17, 35 (1962).
3. A. W. Overhauser, *Phys. Rev.* 128, 1437 (1962).
4. W. M. Lomer, *Proc. Phys. Soc., London* 80, 489 (1962).
5. Y. Hamaguchi, E. O. Wollan, and W. C. Koehler, *Phys. Rev. A* 138, 737 (1965).
6. W. C. Koehler et al., *Phys. Rev.* 151, 405 (1966).
7. S. Arajs and W. E. Katzenmeyer, *J. Phys. Soc. Jpn.* 23, 932 (1967).

8. S. Arajs, E. E. Anderson, and E. E. Ebert, *Nuovo Cimento* 4B, 40 (1971).
9. L. Hedman et al., *Phys. Lett.* 45A, 175 (1973).
10. K. Fukamichi and H. Saito, *J. Phys. Soc. Jpn.* 38, 287 (1975).
11. S. Arajs et al., p. 231 in *Low Temperature Physics—LT 14*, ed. by M. Krusius and M. Vuorio, North Holland Publishing Co., Amsterdam, 1975.
12. A. Jayaraman et al., *Phys. Rev. Lett.* 37, 926 (1976).

MAGNETIC SHORT-RANGE ORDER IN GADOLINIUM[1]

H. R. Child

Quasi-elastic neutron scattering has been used to investigate magnetic short-range order in gadolinium for 80 K $< T <$ 425 K. Short-range order exists throughout this range from well below $T_C =$ 291 K to well above it and can be reasonably well described by an anisotropic Orstein-Zernike form for $\chi(Q)$.

1. Abstract of paper: p. 425 in *Proceedings of the Conference on Neutron Scattering*, vol. 1, ed. by R. M. Moon, ERDA CONF-760601-P1, Oak Ridge, Tenn., 1976.

MAGNETIC FORM FACTOR OF SmS AND $Sm_{0.76}Y_{0.24}S$

R. M. Moon F. Holtzberg[1]
W. C. Koehler D. B. McWhan[2]

Currently interest is high in a class of compounds containing rare earth ions that show apparent nonintegral valences. These mixed-valence compounds have been recently reviewed by Varma.[3] It is thought that the basic factor influencing the behavior of these materials is the coexistence at the Fermi level of ionic-like 4*f* levels and a wide *s-d* conduction band. Through reciprocal electron transfer between the 4*f* levels and the conduction band, the ionic valence can fluctuate between integral values. For experiments that have a characteristic measuring time long compared to the fluctuation time, such as lattice constant and Mössbauer isomer shift measurements, a single quantity is observed with a value intermediate between those expected for the two ionic configurations. For experiments which have a characteristic time that is short compared to the fluctuation time, such as x-ray photoemission spectroscopy, both electronic configurations are observed. The idea of interconfiguration fluctuations has been advanced in a theory due to Hirst.[4]

At atmospheric pressure SmS is a semiconductor with lattice constant and susceptibility characteristic of Sm^{2+}. At about 6 kbar it transforms to a mixed-valence phase with a contraction of the lattice constant of about 5%. From lattice constant and Mössbauer isomer shift measurements,[5] the apparent valence in the collapsed phase is about +2.8. The mixed-valence phase also may be produced chemically at atmospheric pressure by alloying with various elements. The alloy $Sm_{0.76}Y_{0.24}S$ is in the mixed-valence phase at room temperature[6] with an apparent valence of about +2.6. As the temperature is lowered, the lattice expands and the apparent valence shifts to about +2.4.

In an effort to understand the nature of the mixed-valence phase better, in particular the electronic wave functions, we have measured the induced-moment form factor of SmS in both the low- and high-pressure phases and of $Sm_{0.76}Y_{0.24}S$ at temperatures above and below the lattice transition. The polarized neutron technique was employed to measure the elastic magnetic structure factors in an applied field of 42.5 kOe. In these measurements we obtain the Fourier transform of the temporal average of the induced magnetic moment density.

The theory of the magnetic properties of mixed-valence systems is not in good enough shape to allow a prediction; nor will it permit a straightforward interpretation of our results. We can predict the form factors expected for the +2 and +3 Sm ions, and these form factors turn out to be quite different. However, it is clear from the susceptibility measurements of Maple and Wohlleben[7] on the mixed-valence phase of SmS that we should not expect a linear combination of +2 and +3 free-ion form factors. Were this the case, the +3 contribution should cause the susceptibility to diverge at low temperatures. Nevertheless, it is certainly of interest to compare our experimental results with the expected ionic form factors for the two valence states.

The induced-moment form factor for an ionic compound can be written as[8]

$$f(q) = \langle j_0(q) \rangle + c_2 \langle j_2(2q) \rangle , \qquad (1)$$

where $\langle j_n \rangle$ is an integral of the product of the 4*f* radial electron density and a spherical Bessel function of order n, and

$$c_2 \cong \frac{\bar{L}_z}{\bar{L}_z + 2\bar{S}_z} , \qquad (2)$$

where $\bar{L}_z$ denotes the thermal average of L_z (keeping terms linear in the applied field). For Sm^{2+} the ground

state is $^7F_0$ and the low-temperature values of $\bar{L}_z$ and S_z are dominated by the field-induced admixture of the neighboring $^7F_1$ level into the ground state, resulting in the Van Vleck temperature-independent susceptibility. From Eq. (2) and the fact that $\langle J+1, J_z|L_z|J, J_z\rangle = -\langle J+1, J_z|S_z|J, J_z\rangle$ for Russell-Saunders coupling, we conclude that $c_2 \cong -1$ in any ionic case where Van Vleck paramagnetism is dominant. For Sm^{2+} we find that $c_2^{2+} = -5/6$; this value is nearly independent of temperature up to 300 K. For Sm^{3+} the ground state is $^6H_{5/2}$, and at very low temperatures the susceptibility and form factors are dominated by the $1/T$ terms arising from this manifold of states. The characteristic value of c_2 for this manifold is +5.42. A Van Vleck contribution to the Sm^{3+} susceptibility arising from a field-induced admixture of the $J = 7/2$ levels into the ground state also exists. If we could isolate this contribution, we would find a form factor similar to that for Sm^{2+} ($c_2 \cong -1$). Because the Van Vleck contribution comprises more of the total as the temperature is increased, we expect the Sm^{3+} form factor to be strongly temperature dependent. In fact, for the free ion, c_2^{3+} changes from +5.42 at 0 K to +0.85 at 300 K. A cubic crystal field will have a negligible effect on the Sm^{2+} form factor, but may have a profound effect on the Sm^{3+} form factor if it is strong enough to mix the $J = 7/2$ and $J = 5/2$ levels significantly.

With this background, let us examine the experimental results. The only case for which we have definite expectations is SmS at low pressure where Sm^{2+} behavior should be observed. The SmS data (Fig. 4.31) were obtained by using a powder sample prepared at the IBM Thomas J. Watson Research Center and ^{154}Sm supplied by ORNL. The low-pressure form factor is in good agreement with the calculated Sm^{2+} form factor. The data were normalized based on a susceptibility of 10.2×10^{-3} emu/mole, which is in good agreement with measurements by Tao and Holtzberg[6] but somewhat higher than the results of Bucher[9] et al. After completing the low-pressure experiment, the sample was loaded in a pressure cell designed and fabricated at the Bell Laboratories and pressurized above 6 kbar. About 80% of the sample transformed into the collapsed mixed-valence phase. A rather unfavorable signal to background ratio limited the statistical accuracy that could be obtained for the mixed-valence phase, but within the experimental accuracy little difference seems to occur between the low- and high-pressure phases. The high-pressure data were normalized based on a susceptibility of 2.9×10^{-3} emu/mole calculations taken from the work of Maple and Wohlleben.[7]

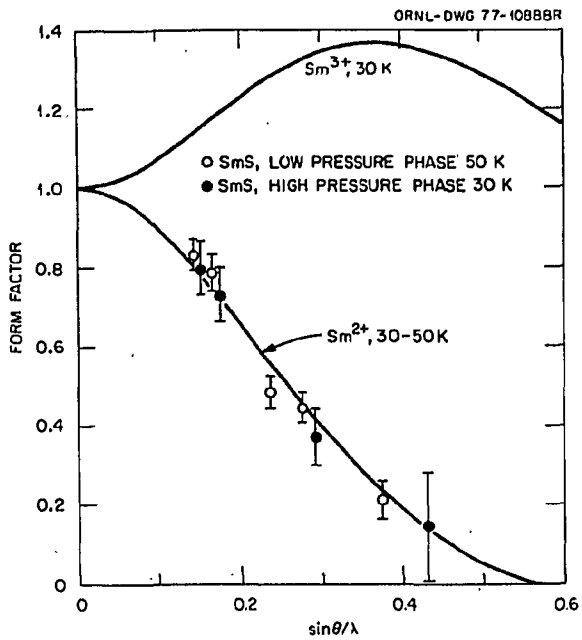

Fig. 4.31. The induced magnetic form factor of SmS in both the normal and mixed valence phases. The calculated curves are for ions in a cubic environment with crystal field and exchange parameters appropriate for SmS.

The alloy data shown in Fig. 4.32 were obtained using a single crystal of $^{154}Sm_{0.76}Y_{0.24}S$ grown at the IBM Thomas J. Watson Research Center. The normalization was based on susceptibility measurements performed on the same sample. Little temperature dependence is evident, and again the data are in fairly good agreement with the Sm^{2+} form factor. The calculated curves shown in Figs. 4.31 and 4.32 were based on excited ionic energy levels at 420 K ($J = 1$) for Sm^{2+} and 1400 K ($J = 7/2$) for Sm^{3+}, a crystal field parameter $A_4\langle r^4\rangle = 110$ K, and an exchange parameter $J(0) = 7.0$ K. The integrals $\langle j_0\rangle$ and $\langle j_2\rangle$ have been calculated for both Sm^{2+} and Sm^{3+} by C. W. Nestor of ORNL using relativistic Dirac-Fock wave functions.

These results show that the form factor for the mixed-valence phase is nearly identical to that expected for the Sm^{2+} ion, independent of whether the mixed valence phase is produced by pressure of alloying. It is as if the +3 configuration made no contribution to the induced moment, or, more precisely, as if the Curie ($1/T$) terms normally associated with the +3 ion made no contribution to the induced moment. If only the Van Vleck terms are

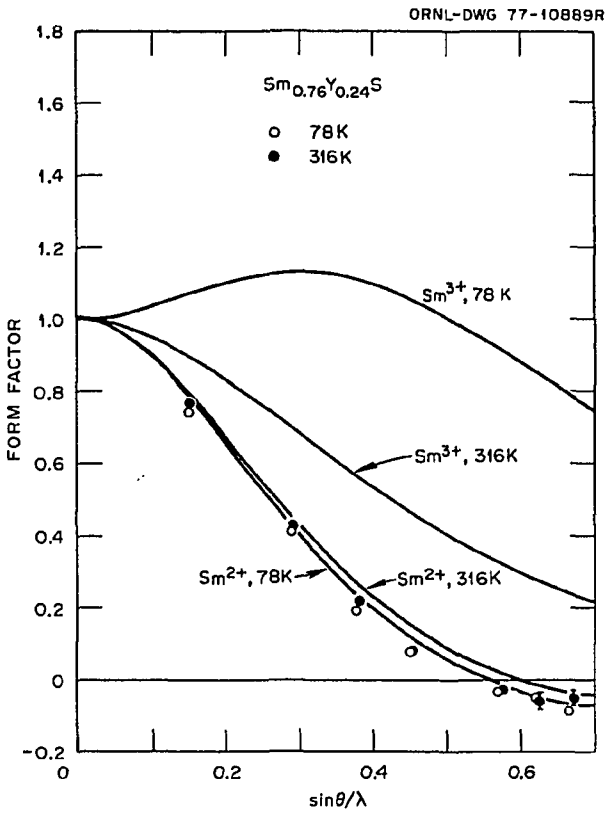

Fig. 4.32. The induced magnetic form factor of $Sm_{0.76}Y_{0.24}S$. Note the dramatic temperature dependence in the calculated curves for Sm^{3+} and the near absence of a temperature dependence in the experimental results.

effective, the +3 form factor would look very much like the +2 form factor. A suppression of the Curie terms is consistent with the observation of no magnetic ordering or divergence of the susceptibility as $T \rightarrow 0$.

Our hope is that when an adequate theory of the magnetic properties of mixed-valence systems is developed, these results will be helpful in verifying the theory. Varma and Yafet[10] have shown qualitatively that the susceptibility for a system like SmS in the mixed valence phase should go like $(T+\Delta)^{-1}$, and Sales and Wohlleben[11] have had some success in calculating the temperature dependence of the susceptibility for some mixed-valence compounds by replacing the thermodynamic temperature T by $T+\Delta$. The effect of this assumption is to decrease the importance of the Curie terms. Some calculations along these lines for SmS are in progress.

1. IBM Thomas J. Watson Research Center, Yorktown Heights, N.Y.

2. Bell Laboratories, Murray Hill, N.J.
3. C. M. Varma, *Rev. Mod. Phys.* 48, 219 (1976).
4. L. L. Hirst, *Phys. Kondens. Mater.* 11, 255 (1970); *J. Phys. Chem. Solids* 35, 1285 (1974); *Phys. Rev. B* 15, 1 (1977).
5. J.M.D. Coey et al., *Phys. Rev. B* 14, 3744 (1976).
6. F. Holtzberg, *AIP Conf. Proc.* 18, 478 (1974); L. J. Tao and F. Holtzberg, *Phys. Rev. B* 11, 3842 (1975).
7. M. B. Maple and D. Wohlleben, *Phys. Rev. Lett.* 27, 511 (1971).
8. C. Stassis and H. W. Deckman, *Phys. Rev. B* 12, 1885 (1975).
9. E. Bucher, U. Narayanamurti, and A. Jayaraman, *J. Appl. Phys.* 42, 1741 (1971).
10. C. M. Varma and Y. Yafet, *Phys. Rev. B* 13, 2950 (1976).
11. B. C. Sales and D. K. Wohlleben, *Phys. Rev. Lett.* 35, 1240 (1975).

MAGNETIC EXCITATIONS IN MIXED-VALENCE $Sm_{0.75}Y_{0.25}S$

H. A. Mook T. Penney[1]

The magnetic scattering from the mixed-valence system can give us direct information about the valence state and fluctuation time of the system. For $Sm^{2+}S$ in a cubic crystalline field, the ground magnetic state is a $^7F_0$ singlet that does not split in the crystalline field. The next multiplet level $^7F_1$ is a triplet that is about 34 meV above the $^7F_0$ level. The $^7F_0 \rightarrow {}^7F_1$ excitations have been studied by Shapiro et al.[2] for pure $Sm^{2+}S$ that is not in the mixed valence state. For $Sm^{3+}S$ the ground state is the $^6H_{5/2}$ configuration. This configuration is split in the crystalline field into a doublet Γ_7 and a quartet Γ_8 that are thought to be on the order of 10 meV apart. The amount of each valence state can then be determined by observing the strength of the magnetic excitations from each configuration. Time-of-flight measurements have been made on powders of both SmS and $Sm_{0.75}Y_{0.25}S$ as a function of temperature. Except for room temperature, single crystals were not used since the samples used in the phonon experiments broke upon warming through the transition; moreover, most of the information of interest can be obtained with the powdered samples. Figure 4.33 shows a plot of the $^7F_0 \rightarrow {}^7F_1$ excitation as a function of temperature for SmS.

The width of the measured line stems from both dispersion of the excitation and spectrometer resolution. At low temperatures the mode dips down at the zone center by around 6 meV but remains at about 36 meV at the zone boundary. As the temperature is increased, the zone center energy increases to a value nearer that of the zone boundary so that the mode becomes flatter at higher temperatures. We sample all momentum values in a powder, with the zone boundary being most heavily

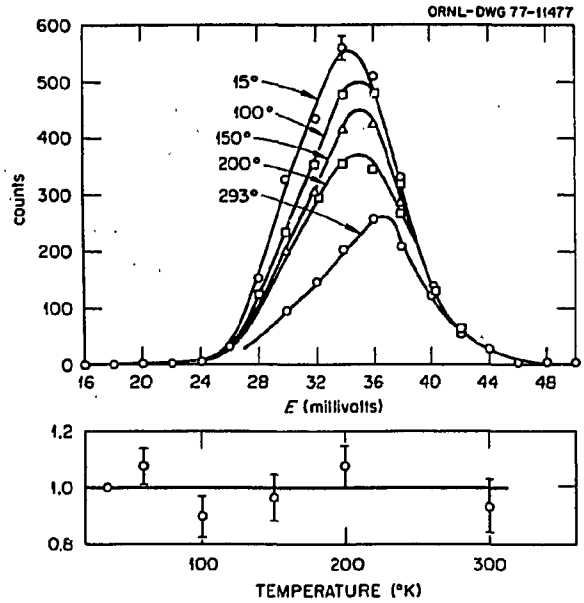

Fig. 4.33. Measurements of the $^7F_0 - {}^7F_1$ transition in SmS powder. The graph at the bottom shows the intensity of the excitation plotted on a scale that is unity if Eq. 1 is followed.

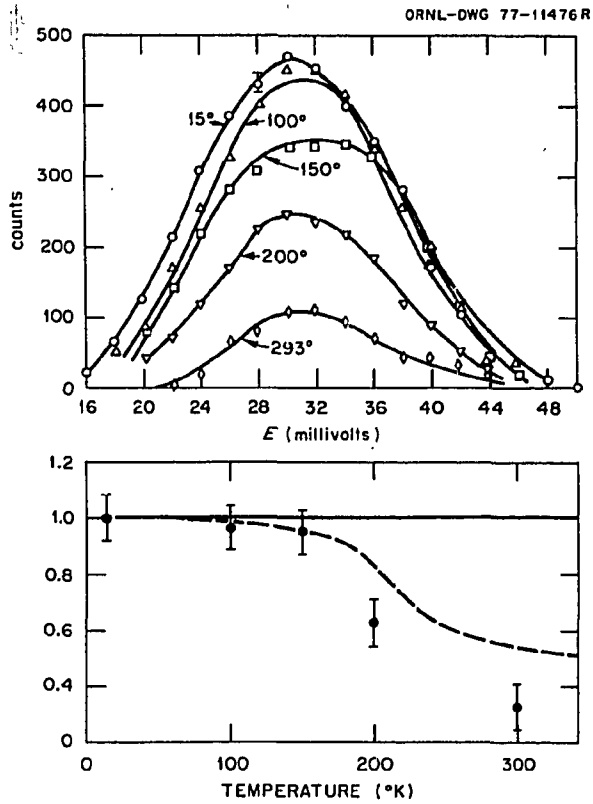

Fig. 4.34. Measurements of the $^7F_0 - {}^7F_1$ transition in $Sm_{0.75}Y_{0.25}S$. A similar intensity plot is shown as in Fig. 4.33. The dashed line is a calculated value for the intensity assuming the S^{2+} to S^{3+} conversion follows the lattice constant.

weighted. One can see the intensity of the peak shifting up to higher energies as the temperature increases, as expected. The line shape is well accounted for by a convolution of the resolution function of the spectrometer and the shape of the dispersion curve; no intrinsic line width is observed. The temperature dependence of the intensity of the line should go like

$$I(t) = \frac{1}{1 + 3[\exp(36.0/k_\beta T)]} . \qquad (1)$$

On the bottom of Fig. 4.33 a plot of the integrated intensities is shown where the intensities are normalized so that they are unity if the relation in Eq. (1) is followed. Satisfactory agreement between the intensities and Eq. (1) is observed so that SmS appears well understood.

Figure 4.34 shows data taken on $Sm_{0.74}Y_{0.25}S$. The results appear similar, but obvious differences exist. The excitation appears much broader in energy, and the temperature dependence does not follow Eq. (1). As the temperature is increased, the intensity decreases rapidly; a plot of the integrated intensity normalized to Eq. (1) is shown (Fig. 4.34). Clearly the $Sm^{2+}S$ transition is getting smaller faster than the result given by Eq. (1); this transition can be understood if some of the material is converting from Sm^{2+} to Sm^{3+} when the temperature is increased. The dashed line shows the strength of transition expected if the conversion of the material from Sm^{2+} to Sm^{3+} follows the value calculated from the lattice constant extrapolation. The agreement is close, but the intensity appears to fall off somewhat faster than expected. Of course, the lattice constant extrapolation may not be a very accurate measure of the valence state of the material. It seems clear, however, that the valence state of the material is a function of temperature, much as expected from lattice constant, photoemission, and Mössbauer measurements. A search for the Sm^{3+} transition between the Γ_7 and Γ_8 levels was unsuccessful despite the fact that the transition probability between the two states is large. However, if this transition were smeared out in energy in a fashion similar to the Sm^{2+} transition, it probably would be unobservable.

The exact origin of the large line width of the Sm^{2+} transition is not known. One possibility would be that it comes from increased dispersion. We have ruled

this out at room temperature by making both time-of-flight and triple-axis measurements on single crystals. We again find line widths similar to those found in Fig. 4.34, but dispersion is not significantly different from that found for SmS. A more likely explanation can be based on the fluctuation time between the Sm^{2+} and Sm^{3+} states. The x-ray photoemission results suggest a time below 10^{-15} sec, while the Mössbauer measurements give a time larger than 10^{-9} sec. Using the uncertainty principle $\Delta E \Delta t \sim h$, we obtain a time of about 5×10^{-13} sec for the observed line width of about 10 meV. This is the first direct observation of the valence fluctuation rate in the mixed-valence materials.

1. IBM Thomas Watson Research Center, Yorktown Heights, N.Y.

2. S. M. Shapiro, R. J. Birgeneau, and E. Bucher, *Phys. Rev. Lett.* 34, 470 (1975).

INELASTIC NEUTRON SCATTERING MEASUREMENTS ON $CeAl_3$ AND $Ce_{0.8}Th_{0.2}$[1]

A. S. Edelstein[2] T. Brun[3]
R. Majewski[2] C. A. Pelizzari[3]
S. K. Sinha[3] H. R. Child

Inelastic neutron scattering measurements have determined that the spectrum of $Ce_{0.8}Th_{0.2}$ at 170 K consists of a single quasi-elastic peak of width $\Gamma \cong 12$ meV. Besides a narrower quasi-elastic peak, the spectrum of $CeAl_3$ also shows a crystal field splitting of approximately 5 meV. The temperature dependence of the width Γ of the quasi-elastic peak for each system is best fitted by a model that includes an intrinsic relaxation mechanism as well as the Korringa mechanism. The magnitude of Γ also indicates the hybridization of the cerium moment with the conduction electrons.

1. Abstract of paper: p. 873 in *Proceedings of the Conference on Neutron Scattering*, vol. II, ed. by R. M. Moon, ERDA CONF-760601-P2, Oak Ridge, Tenn., 1976.

2. University of Illinois, Chicago; Argonne National Laboratory, Argonne, Ill.

3. Argonne National Laboratory, Argonne, Ill.

DIFFUSE NEUTRON SCATTERING MEASUREMENTS OF THE FRACTIONAL OCCUPANCY OF THE LOCALIZED $4f^1$ CONFIGURATION IN Ce-Th AND $CeAl_3$[1]

A. S. Edelstein[2] H. R. Child
C. Tranchita[3]

Diffuse neutron scattering measurements at $2 < T < 300$ K have been employed to determine the fractional occupancy η of the localized $4f^1$ configuration. For $CeAl_3$, $\eta = 0.9$–1.0 at 11 K. For $Ce_{0.8}Th_{0.2}$, $\eta = 0.4 \pm 0.1$ at 11 K. No evidence of a compensating conduction electron polarization was observed.

1. Abstract of paper: *Phys. Rev. Lett.* 36, 1332 (1976).

2. University of Illinois, Chicago; Argonne National Laboratory, Argonne, Ill.

3. University of Illinois, Chicago.

NEUTRON SCATTERING STUDY OF THE SPIN DYNAMICS AND SPIN WAVE FORM FACTOR OF CHROMIUM[1]

S. K. Sinha[2] C. Stassis[3]
G. R. Kline[3] N. Chesser[4]
N. Wakabayashi

The spin excitations in a single crystal of $Cr_{0.98}Mn_{0.02}$ have been studied by inelastic neutron scattering. High-resolution triple-axis spectrometer measurements have yielded a value of the spin wave velocity at $T/T_N \cong 0.5$ of $(1.30 \pm 0.15) \times 10^7$ cm/sec in good agreement with earlier measurements. The excitation strength drops extremely rapidly in the vicinity of T_N and decreases approximately linearly above T_N. The spin wave form factor has been measured below and above T_N by measuring the spin wave intensity at various superlattice points and is found to agree to within experimental error with the static spin form factor. The implications of these results for the theory of itinerant electron antiferromagnetism are discussed.

1. Abstract of paper: *Phys. Rev. B* 15, 1415 (1977).

2. Iowa State University, Ames. Present address: Argonne National Laboratory, Argonne, Ill.

3. Iowa State University, Ames.

4. Iowa State University, Ames. Present address: National Bureau of Standards, Washington, D.C.

SPIN WAVES IN AN INVAR ALLOY ($Fe_{0.65}Ni_{0.35}$)[1]

M. Kohgi[2] Y. Ishikawa[2]
N. Wakabayashi

The spin wave dispersion relation in an Invar alloy $Fe_{0.65}Ni_{0.35}$ has been measured at 4.2 K in the [111] direction by neutron inelastic scattering. Well-defined magnon groups have been observed up to an energy transfer of about 80 meV. The spin wave dispersion is well described by $\hbar\omega = Dq^2(1 - \beta q^2)$ with $D = 143$ meV Å^2 and $\beta = 0.12$ Å^2. The value of D is in accord with the value extrapolated from other neutron scattering results at higher contents of nickel and disagrees with spin wave resonance results. No trace of gamma-iron-type antiferromagnetic order could be detected at 4.2 K in this alloy by elastic neutron scattering measurements.

1. Abstract of paper: *Solid State Commun.* 18, 509 (1976).
2. Tohoku University, Sendai, Japan.

SPIN WAVES IN FERROMAGNETIC $Tb_{0.76}Y_{0.24}$

N. Wakabayashi R. M. Nicklow
H. R. Child

The conduction electron susceptibility $\chi(q)$ is considered to play an important role in the magnetism of rare earth metals and alloys. To obtain information about $\chi(q)$, studies of the spin waves in the alloy system Tb_xY_{1-x} have been continued in a magnetic field.

The magnetic structure of the alloy with $x = 0.76$ was found to remain spiral down to liquid helium temperature in zero field. The spin wave dispersion curve in this structure has already been studied along the c^*-direction, and the results were analyzed[1] successfully in terms of a susceptibility function corresponding to a one-dimensional system with a slight modification. To obtain somewhat independent information about $\chi(q)$, the spin wave dispersion curve for the ferromagnetic phase has been studied. A field of 15 kG was necessary to transform the structure from spiral to ferromagnetic at liquid helium temperature. Results for the dispersion curve measurements are summarized in Fig. 4.35. Spin wave energies that are calculated in terms of the susceptibility function determined from the measurements in the spiral structure (solid line in Fig. 4.35) agree rather well with the observed energies. Attempts will be made to construct a model that gives better consistency between spin wave energies for the spiral structure and those for the ferromagnetic structure. As is shown in Fig. 4.36, a

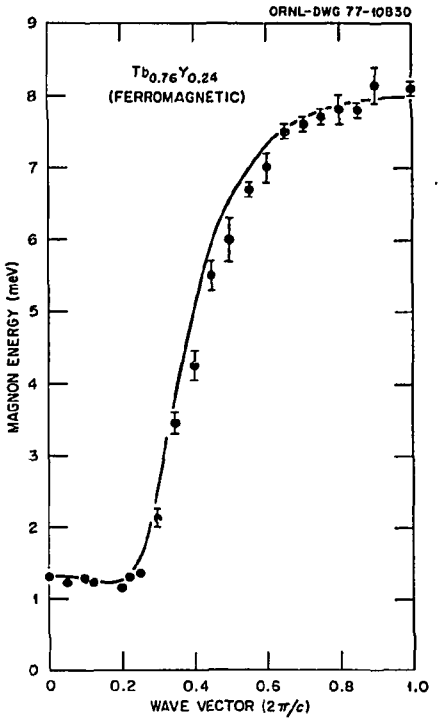

Fig. 4.35. Spin wave dispersion curve along the c^*-direction for ferromagnetic $Tb_{0.76}Y_{0.24}$. An external magnetic field of 15 kG was applied to obtain the ferromagnetic structure. The solid line represents the calculation performed on the basis of the information derived from spin waves in the spiral structure.

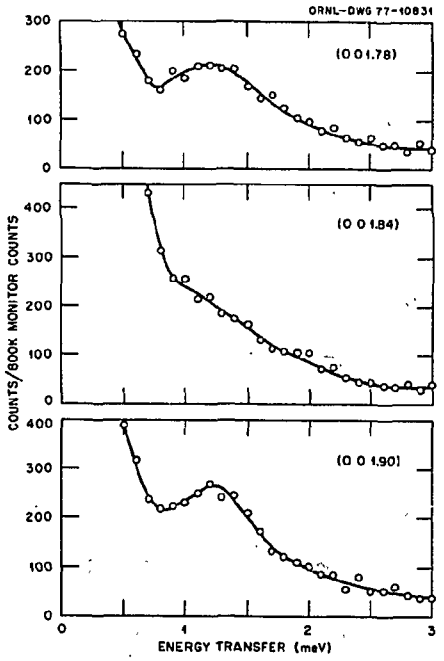

Fig. 4.36. Scattered neutron groups for wave vectors near the wave vector characterizing the spiral configuration. No well-defined peak could be observed for $q = 0.16$.

large damping and softening of the spin wave has been observed near the wave vector q = 0.16, which characterized the spiral configuration. The origin of the phenomenon may be related to the instability of the ferromagnetic structure, but it is not clearly understood at present.

1. N. Wakabayashi and R. M. Nicklow, p. 789 in *Proceedings of the Conference on Neutron Scattering*, vol. II, ed. by R. M. Moon, ERDA CONF-760601-P2, Oak Ridge, Tenn., 1976.

SPIN WAVE DISPERSION IN Tb-Y ALLOYS[1]

N. Wakabayashi R. M. Nicklow

The alloys Tb_cY_{1-c} ($0.05 \lesssim c \lesssim 0.85$) have spiral magnetic structures with the moments confined to the plane parallel to the basal plane of the hexagonal structure. The spin wave dispersion curves along the c^*-direction have been measured for alloys with $c =$ 0.1, 0.5, 0.76, and 0.85. Some of the results are shown in Fig. 4.37.

In the mean lattice approximation the dispersion relation along the c^*-direction is given by

$$E(q) = J\Big(\{c\mathcal{J}(q_0) - (c/2)[\mathcal{J}(q_0+q) + \mathcal{J}(q_0-q)]\} \times [c\mathcal{J}(q_0) - c\mathcal{J}(q) + 2B]\Big)^{1/2} , \quad (1)$$

where J is the angular momentum, c is the concentration of magnetic atoms, B is the axial anistropy constant, and q_0 is the wave vector that specifies the periodicity of the spiral structure. The RKKY exchange interaction $\mathcal{J}(q)$ is proportional to the generalized susceptibility $\chi(q)$ of the conduction electrons. The microscopic calculations of $\chi(q)$ for yttrium indicate the existence of a prominent peak due to the nesting of the Fermi surface which may be retained to some extent in the alloys. Thus the data were analyzed on the basis of a susceptibility function which is similar to that for a one-dimensional system with a modification due to the incomplete nesting. The functional form chosen is

$$\chi(q) \propto \frac{2k_F q}{q^2 + (\gamma q^2)^2} \log \left| \frac{(2k_F+q)^2 + (\gamma q^2)^2}{(2k_F-q)^2 + (\gamma q^2)^2} \right| , \quad (2)$$

where γ is a measure of the incompleteness of the nesting. P specifies the scale factor between $\mathcal{J}(q)$ and $\chi(q)$; P, γ, and k_F are the fitting parameters of the model. This form of $\chi(q)$ was found to give reasonable fits to the data for all the values of c, as is seen in Fig. 4.37. However, because this form has

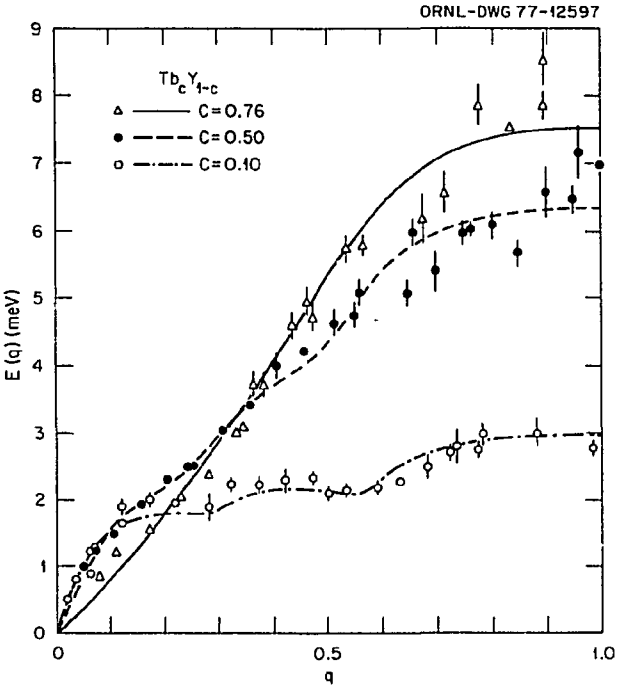

Fig. 4.37. Spin-wave dispersion curves for Tb-Y alloys along the c^*-direction.

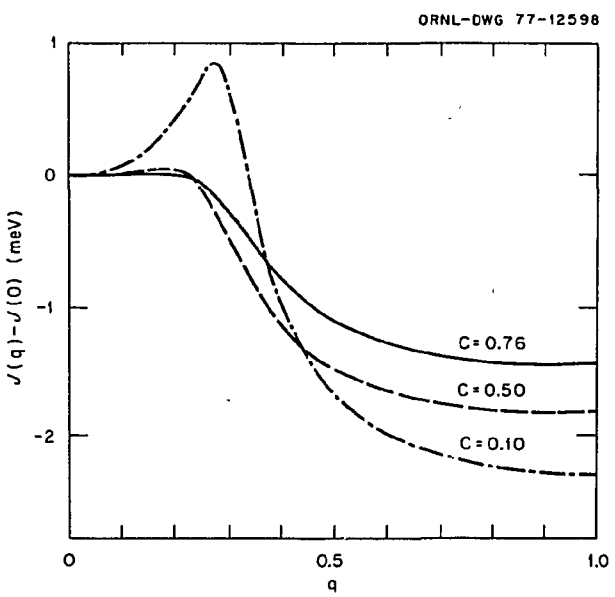

Fig. 4.38. Exchange function for Tb-Y alloys.

only one peak (Fig. 4.38), it cannot reproduce the second peak known to exist in $\mathcal{J}(q)$ near $q = 0.8$ for pure terbium. Thus it is perhaps necessary to introduce more parameters in the present model,

which may not be any more advantageous than the conventional Fourier series analysis.

1. Summary of paper: p. 789 in *Proceedings of the Conference on Neutron Scattering*, vol. II, ed. by R. M. Moon, ERDA CONF-760601-P2, Oak Ridge, Tenn., 1976.

SPIN WAVES IN THE CUBIC FERRIMAGNET $Ho_{0.88}Tb_{0.12}Fe_2$[1]

R. M. Nicklow C. M. Williams[2]
N. C. Koon[2] J. B. Milstein[2]

Using neutron spectrometry, we have investigated the magnon dispersion relation for the ferrimagnetic cubic Laves compound $Ho_{0.88}Tb_{0.12}Fe_2$ at room temperature and at 12 K. The results are described surprisingly well by a very simple near-neighbor exchange model that includes only iron-iron and iron-rare earth interactions, crystal field anisotropy, and temperature renormalization that is derived from the sublattice magnetization.

1. Abstract of paper: *Phys. Rev. Lett.* 36, 532 (1976).
2. Naval Research Laboratory, Washington, D.C.

MAGNETIC EXCITATIONS IN AMORPHOUS $Fe_{75}P_{15}C_{10}$[1]

H. A. Mook C. C. Tsuei[2]

Neutron scattering techniques have been used to measure the magnetic excitations in the amorphous ferromagnet $Fe_{75}P_{15}C_{10}$. Triple-axis measurements show a distinct spin wave excitation at small momentum transfers that closely obeys a quadratic dispersion relation $E = DQ^2$ for D equal to about 120 meV Å^2. Time-of-flight polarized beam measurements made in the vicinity of the first peak in $S(Q)$ near 3 Å^{-1} show excitations that reach a minimum energy at the maximum in $S(Q)$. These excitations are similar to the roton excitations in ^{4}He except that they are rather broad in energy since they are able to decay into single particle states. A contour map that shows the scattering measurements in the neighborhood of 3 Å^{-1} is presented in the report, and the results are compared with calculations of magnetic excitations in amorphous systems.

1. Abstract of paper: *Physical Review B* (in press).
2. IBM Thomas J. Watson Research Center, Yorktown Heights, N.Y.